Smart Structures and Systems, *Vol. 28, No. 1 (2021) 121-142*
https://doi.org/10.12989/sss.2021.28.1.121

Identification and evaluation of cracks in electrostatically actuated resonant gas sensors using Harris Hawk / Nelder Mead and perturbation methods

Behnam Firouzi, Ahmad Abbasi and Polat Sendur*

Vibrations and Acoustics Laboratory (VAL), Mechanical Engineering Department, Ozyegin University, Istanbul, Turkey

(*Received September 9, 2020, Revised March 9, 2021, Accepted March 22, 2021*)

Abstract. In this paper we study the static deflection, natural frequency, primary resonance of an electrostatically actuated cracked gas sensor. Besides, a novel hybrid metaheuristic algorithm is proposed to detect the location and depth of possible crack on the microcantilever systems. The gas sensor configuration consists of a microcantilever with a rigid plate attached to its end. The nonlinear effects of the electrostatic force and fringing field are taken into account in the mathematical model. The crack is represented by a rotational spring. In the first part, the effect of crack on the static and dynamic pull-in instability are studied. The equations of motion are solved by the application of the perturbation methods. Next, an inverse problem is formulated to predict the location and depth of the crack in the gas sensor. For that purpose, the weighted squared difference of the analytical and predicted frequency response is considered as the objective function. The location and depth of the crack in the microsystem are determined using the hybrid Harris Hawk and Nelder Mead optimization algorithms. The accuracy and efficiency of the proposed algorithm are compared with the HHO, DA, GOA, and WOA algorithms. Taguchi design of experiments method is used in order to tune the parameters of optimization algorithms systematically. It is shown that the proposed algorithm can predict the exact location and depth of the open-edge crack on an electrostatically actuated microbeam with proof mass.

Keywords: crack; MEMS; metaheuristic algorithm; Nelder Mead; optimization HHO; pull in instability

1. Introduction

Electrostatically actuated sensors are frequently used in many applications, especially in the fields of chemistry, biology and, physics. Micro Electro Mechanical Systems (MEMS) sensors are classified as resonators and non-resonance sensors. In the latter, a movable electrode (microcantilever) deflects towards the fixed opposing electrode by the application of the DC voltage between them. In mass sensors and pollutant sensors, the microcantilever is deformed, and the capacity of the capacitor comprising two electrodes is changed by attracting the mass or pollutant. Therefore, by measuring the changes in the capacity, the level of pollution or mass can be measured. In the resonant sensors the combination of DC and AC voltage is applied between the micro-beam and opposite electrode. The electrostatic force due to DC component deflects the micro-beam to a new position, while AC component vibrates the micro-beam around this equilibrium position. In these systems, the measurements are performed by monitoring the changes in the resonant frequency due to the nonlinear jump phenomenon. A change in the stiffness or mass of the system shifts the resonance frequency of the resonator or creates a sudden change on the response. The amount of the frequency or response shift may be taken as a direct measurement of the physical parameter. The performance of these systems highly depends on the frequency response characteristics and the resonance frequencies (Younis 2011).

One of the main causes of failure in the electrostatically actuated systems is due to the pull-in instability. The pull-in instability occurs when the elastic restoring force of the microbeam is incapable of resisting against the electrostatic force, and consequently coming in contact with the opposite electrode. There has been a vast body of literature on the effect of pull-in instability on the performance of microsystems (Bianchi and Radi 2020, Duan and Rach 2013, Zamanian *et al*. 2018, Bansal *et al*. 2020, Abdalla *et al*. 2005, Zhang and Fu 2012). Another important factor affecting the performance of MEMS sensors and actuators is cracks on the microbeams. The cracks can develop as a result of the manufacturing and machining processes as well as during the operation of the sensors. Cracks increase the local flexibility of microbeam due to increased stress concentration. Therefore, cracks can affect the static and dynamic pull-in behavior, and thereby the stability of the MEMS devices.

Sourki and Hoseini (2016) studied the effect of crack parameters on the transverse vibration of cracked Euler Bernoulli microbeam using modified couple stress theory. They concluded that these parameters significantly affect the natural frequency of the system. Similarly, Zhou *et al*. (2015) studied the influence of slant cracks on the static and dynamic features of electrostatically actuated microbeams. The study concluded that the effect of crack position is

*Corresponding author, Assistant Professor,
E-mail: Polat.sendur@ozyegin.edu.tr

http://www.techno-press.org/?journal=sss&subpage=7
ISSN: 1738-1584 (Print), 1738-1991 (Online)

more significant than the crack depth. The effect of the crack on the static and dynamic pull-in instability of microbeams with different boundary conditions is considered by Motallebi *et al*. (2012). In this study, the governing static and dynamic equations of motion are solved using SSLM and Galerkin methods. The study concluded that the dimension and location of the cracks had significant influence on the pull-in voltage. The effect of crack on the dynamic characteristics of electrostatically actuated beams is examined by Hassannejad and Amiri Jahed (2018) taking into account the residual stress and fringing field effects. In several studies, the effect of crack position and depth on the mechanical behavior of MEMS/NEMS beams has been studied. For instance, Akbas (2018) used the modified couple stress theory to study the influence of crack parameters on FGM microbeams. In another study, Al-Basyouni *et al*. (2015) studied the bending and vibration of FGM microbeams using modified couple stress theory and neutral surface position methods. In another study, Dastjerdi and Abbasi (2019) employed the transfer matrix method to analyze the behavior of AFM with the open crack. Similarly, the mechanical behavior of cracked nano-beams composed of nanocrystalline materials was considered by Shaat *et al*. (2016) by using a size-dependent micromechanical model and Mindlin couple stress theory.In numerous studies, microbeams with proof mass are used as sensors, actuators, and resonators (Nayfeh *et al*. 2010, Ouakad 2015, Ouakad and Younis 2008, Khater *et al*. 2014, Firouzi *et al*. 2016, Firouzi and Zamanian 2019). Nayfeh *et al*. (2010) proposed a new model of a gas sensor consisting of an electrostatically actuated microcantilever with a rigid plate attached to its end using Galerkin and finite difference methods. In another study, (Ouakad 2015, Ouakad and Younis 2008) investigated the effect of the capillary and mechanical shock on the performance of the gas sensors. Mechanical behavior of binary gas sensor with same configuration, which utilized static bifurcation-based sensing and binary detection, was investigated and validated experimentally by Khater *et al*. (2014).

Since cracks can lead to sudden failure of systems, many research studies attempted to develop new methods to predict the location and depth of crack (Rajabi *et al*. 2017, Huang *et al*. 2017, Vakil-Baghmisheh *et al*. 2008, 2012, Moradi *et al*. 2011, Jena and Parhi 2015, Jena *et al*. 2015, Moezi *et al*. 2015, 2018b). In several studies, optimization algorithms are used to detect the possible crack in a simple beam by considering the problem as an inverse problem and considering the objective function as the weighted squared difference between the measured and calculated natural frequencies, and the depth and location of the crack are taken as optimization variables. Vakil-Baghmishe *et al*. (2008) used binary and continuous forms of Genetic Algorithms (GA) in order to identify the depth and location of cracks in the cantilever beams. In another study, Baghmishe *et al*. (2012), a hybrid algorithm using particle swarm (PS) and Nelder-Mead (NM) algorithm was proposed to detect cracks in the cantilever beams with improved accuracy. Bees Algorithm was used to detect cracks in cantilever beams, where the crack is modelled by a rotational spring (Moradi *et al*. 2011). The study concluded that Bee algorithm can predict the crack location more accurately compared to the particle swarm optimization (PSO) algorithm. (Jena *et al*. 2015) used Self Adaptive Fuzzy PSO algorithm to investigate its applicability for crack identification problems. Moezi *et al*. (2015) predicted the depth and location of crack in cantilever beams by using Modified Cuckoo optimization algorithm (MCOA). While the methodology was accurate in terms of detecting cracks in beams, the number of function evaluations was more than 26,000. Therefore, the authors proposed the application of generalized modified cuckoo optimization algorithm to reduce number of function evaluations in another study (Moezi *et al*. 2015). Besides, detecting the cracks in operational systems has a significant importance in engineering applications. There is a various array of studies on the crack detection of rotor systems when system is in operation (Xiang *et al*. 2008, He *et al*. 2001, Zhang *et al*. 2016). Tables 1 and 2 give a summary of the related novel techniques for prediction and crack detection using optimization methods, respectively.

Optimization methods have been used in a large number of engineering problems in order to improve the performance of systems or to predict the failure of the systems or medical diagnostics (Deng *et al*. 2019, Cheng *et al*. 2016, He *et al*. 2018a, b, Cao *et al*. 2019a, b, Chen *et al*. 2017). Adaptive differential evolution algorithm using a combined strategy was proposed by Sun *et al*. (2019). Multi-objective optimization algorithms were used in many practical problems in order to optimize different objective functions simultaneously (Amouzgar *et al*. 2020, Cao *et al*. 2019a, 2020b, c, d). Harris Hawk optimization algorithm (HHO) (Heidari *et al*. 2019) is inspired from the modelling of Harris hawk's behavior. The essence of the algorithm is the co-operation between hawks in hunting their prey. More specifically, the attacking strategy of Harris Hawks simultaneously from various directions has been the building block of the algorithm. This algorithm has been demonstrated successfully due to improved exploitation and exploration phases in engineering problems (Abbasi *et al*. 2019, Ekinci *et al*. 2019, Too *et al*. 2019, Yildiz *et al*. 2019a, Aleem *et al*. 2019). Multi population differential

Table 1 Novel techniques for prediction

Study	Methodology	Description
Roy *et al*. 2020	ANFIS-Firefly optimization algorithm	Predict reference evapotranspiration
Chen *et al*. 2018	Multi-criteria decision making	evaluation of shale gas supply chains
Wang *et al*. 2017	Chaotic Moth Flame Optimization	Medical diagnostics
Shen *et al*. 2016	SVM hybrid with firefly optimization algorithm	Medical diagnostics
Cao *et al*. 2020c	Improved Whale optimization algorithm	Parameter estimation
Liu *et al*. 2019	Genetic Algorithm Simulated Annealing	Minimum Energy Consumption

Table 2 Optimization based crack detection in mechanical systems

Study	Methodology	Case	Modelling
Sahoo and Maity (2007)	Hybrid of Genetic Algorithm and artificial neural network (GA-ANN)	Clamped Free Beam and Simple Plane Frame	Finite element model
Sutar *et al*. (2021)	Genetic Algorithm (GA)	Simple Cantilever Beam	Experimental data
Khatir *et al*. (2018)	Particle Swarm Optimization (PSO)	Beam like structures	Finite element model and experimental data
Rezaiee-Pajand and Tavakoli (2015)	Genetic Algorithm (GA)	Concrete gravity dams	Finite element model
Pawar and Gauguli (2003)	Genetic Algorithm (GA) & Fuzzy	Simple Cantilever Beam	Finite element model
He and Hwang (2006)	Hybrid of genetic Algorithm and simulated annealing (GA-SA)	Beam Structures	Finite element Software (ANSYS)
Vakil-Baghmisheh *et al*. (2008)	Continuous Genetic Algorithm (CGA)	Simple Cantilever Beam	Analytical Method (Continuous model)
Moradi *et al*. (2011)	Bee Algorithm (BeA)	Simple Cantilever Beam	Analytical Method (Continuous model)
Vakil-Baghmisheh *et al*. (2012)	Hybrid of Particle Swarm Optimization and Genetic Algorithm (PSO-NM)	Simple Cantilever Beam	Analytical Method (Continuous model)
Moezi *et al*. (2015)	Modified Cuckoo Optimization Algorithm (MCOA)	Simple Cantilever Beam	Analytical Method (Continuous model)
Jena and Parhi (2015)	Modified Particle Swarm Optimization (MPSO)	Simple Cantilever Beam	Analytical Method (Continuous model)
Jena *et al*. (2015)	Adaptive Particle Swarm Optimization (APSO)	Simple Cantilever Beam	Analytical Method (Continuous model)
Moezi *et al*. (2018a)	Generally Modified Cuckoo Optimization Algorithm (GMCOA)	Simple Cantilever Beam	Analytical Method (Continuous model)

evaluation-assisted Harris Hawk optimization method was proposed by Chen *et al*. (2020) to improve the exploitation and exploration performance of HHO algorithm.

The microcantilever with tip mass introduced by Nayfeh *et al*. (2010) has many applications in MEMS, and therefore the capability of detecting crack parameters in such systems is of engineering importance. In this study, first the effect of the crack on the static and dynamic performance of the aforementioned microsystems are investigated. The equations of motion are derived using Newton's method, and the static deflection and natural frequency of the beam are obtained analytically. The dynamic performance of the system is determined using the multiple scale perturbation method, which can determine the unstable region in the frequency response curve. This feature of the algorithm makes it more attractive than the other numerical methods. In the second part of the paper, a novel optimization-based method is proposed to determine the location and depth of the gas sensors using the modal characteristics of the system. The performance of the proposed hybrid algorithm is compared with algorithms commonly used in the literature. Although there are research studies on the application of the metaheuristic algorithms to detect cracks to simple beams, this is the first application of the aforementioned metaheuristic algorithms to the MEMS systems to the author's best knowledge. In addition, the existence of the force due to electrostatic actuation makes the current study more challenging. Since the nonlinearity due to electrostatic force and fringing field effects are taken into consideration in the proposed study, the cost function becomes more complex compared to the common modelling approaches in the literature in which the force and momentum terms are ignored. Besides, the existence of the electrostatic force has a softening effect thereby changing the mechanical characteristics of the system. The objective of this paper is to present a novel algorithm that is able to detect the crack position and depth accurately for the electrostatically actuated gas sensors with an open edge crack.

The paper is organized as follows: first, mathematical model of the electrostatically actuated cracked microbeam with tip mass is explained in Section 2. Furthermore, the static deflection, natural frequency and nonlinear dynamics are presented in this section. The effect of the crack on the static and dynamic pull-in instability is analyzed in Section 3. Section 4 is reserved for the analysis of the effect of crack on the natural frequencies of the microcantilever. Crack identification methodology using inverse approach is presented in Section 5. The performance of the HHO algorithm and the proposed hybrid algorithms is compared in Section 6. The comparison with the optimization algorithms from the literature is presented in Section 7. Finally, the conclusions are given in Section 8.

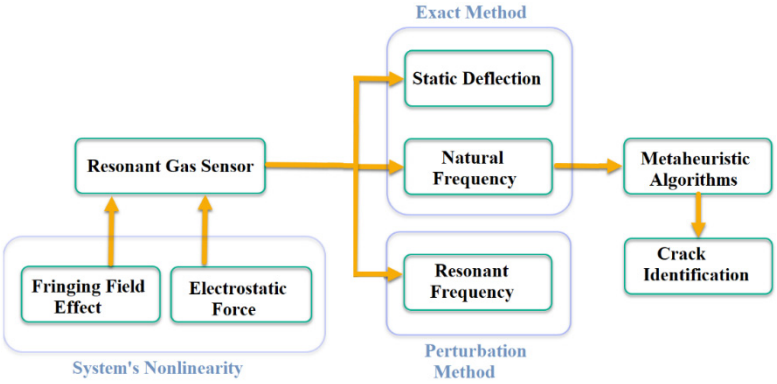

Fig. 1 A general flowchart for the proposed algorithm

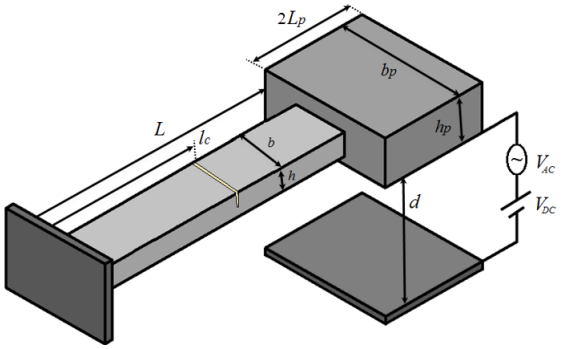

Fig. 2 Schematic view of microsystem and its parameters

2. Modelling and formulation

A general flowchart of study is shown in Fig. 1. There are two sources of nonlinearity: 1) electrostatic force, and 2) fringing field effect. The static deflection, natural frequency and primary resonance of the system with crack are determined analytically. Then, the weighted squared difference of the measured and calculated natural frequency is used as the objective function. Finally, the location and depth of possible crack are estimated using metaheuristic algorithms.

The configuration of the micro-gas sensor, which is shown in Fig. 2, consists of a cantilever micro-beam with length of L and a rigid plate attached to its free end. There is a transverse open-edge full-width crack of depth d_c, at position l_c. The crack is oriented perpendicular to the longitudinal axis of the microbeam.

The system can be modelled by two uniform sections, representing the part of the beam before and after the crack (section 1 and 2 in Fig. 3(a)), that are connected to each other with a rotational spring. The DC voltage, V_{DC}, is applied between the rigid plate and the electrode plate, which is located at a distance d from the microplate. The free body diagrams of the aforementioned microbeam in the original and deflected configurations are shown in Fig. 3(a) and 3(b), respectively. In this model, w_1 and w_2 describe the transverse displacement of the beam on the left and right sides of the crack, respectively. Similarly, w_3 is the transverse displacement of the rigid microplate. The shear force, F_{eq}, and the bending moment, M_{eq}, at the free end of the microbeam are included in the equation of motion using a Dirac delta function. The governing equations of motion for the beam before and after the crack, and boundary conditions using Euler-Bernoulli beam formulation are summarized as follows (Hagedorn and DasGupta 2007)

$$\begin{aligned} &EI\frac{\partial^4 w_1}{\partial x^4}+\rho A\frac{\partial^2 w_1}{\partial t^2}+c\frac{\partial w_1}{\partial t}=0 \qquad 0\le x\le l_c \\ &I\frac{\partial^4 w_2}{\partial x^4}+\rho A\frac{\partial^2 w_2}{\partial t^2}+c\frac{\partial w_2}{\partial t} \\ &=F_{eq}\delta(x-l)+M_{eq}\frac{\partial\delta(x-l)}{\partial x} \qquad El_c\le x\le L \end{aligned} \tag{1}$$

$$\begin{aligned} &w_1|x=0=0, \qquad \frac{\partial w_1}{\partial x}|x=0=0, \\ &\frac{\partial^2 w_2}{\partial x^2}|x=L=0\ |x=L, \\ &\frac{\partial^3 w_2}{\partial x^3}|x=L=0\ |x=L \end{aligned} \tag{2}$$

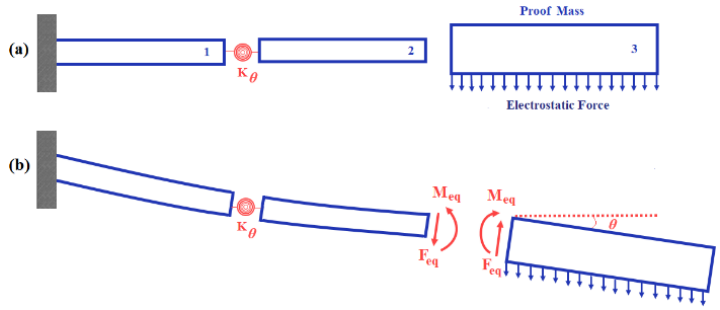

Fig. 3 Free body diagram of system (a) original; and (b) deflected configurations

The continuity equations between the left and right sides of crack are given as follows

$$\begin{aligned} &w_1|x=l_c = w_2|x=l_c,\\ &\frac{\partial^2 w_1}{\partial x^2}|x=l_c = \frac{\partial^2 w_2}{\partial x^2}|x=l_c\\ &\frac{\partial^3 w_1}{\partial x^3}|x=l_c = \frac{\partial^3 w_2}{\partial x^3}|x=l_c,\\ &EI\frac{\partial^2 w_2}{\partial x^2}|x=l_c = K_\theta\left(\frac{\partial^2 w_2}{\partial x^2}|x=l_c - \frac{\partial^2 w_1}{\partial x^2}|x=l_c\right) \end{aligned} \tag{3}$$

The constant of rotational spring (K_θ) depends on the material and cross sectional geometry of the beam, which can be obtained as follows (Vakil-Baghmisheh *et al*. 2012)

$$K_\theta = \frac{EI}{6(1-\nu^2)h}\times\frac{1}{J} \tag{4}$$

where J is the geometrical factor as given in Eq. (5) (Vakil-Baghmisheh *et al*. 2012)

$$\begin{aligned} J = 1.8624\left(\frac{d}{h}\right)^2 - 3.95\left(\frac{d}{h}\right)^3 + 16.375\left(\frac{d}{h}\right)^4 - 37.226\left(\frac{d}{h}\right)^5 + 76.81\left(\frac{d}{h}\right)^6\\ -126.9\left(\frac{d}{h}\right)^7 + 172\left(\frac{d}{h}\right)^8 - 143.97\left(\frac{d}{h}\right)^9 + 66.56\left(\frac{d}{h}\right)^{10} \end{aligned} \tag{5}$$

Applying Newton's second law for the Fig. 2 yields Eq. (6)

$$\begin{aligned} F_{eq} &= F_{el} + F_{fr} - m_p\frac{\partial^2 w(L,t)}{\partial t^2} - \int_L^{L+2l_p} c\dot{w}_3\ dx\\ M_{eq} &= M_{el} + M_{fr} - I_p\frac{\partial^3 w(L,t)}{\partial x\partial t^2}\\ &\quad - \int_L^{L+2l_p} c(x-(L+L_p))\dot{w}_3\ dx \end{aligned} \tag{6}$$

where the force and torque due to the electrostatic actuation considering the fringing field effects (Vakil-Baghmisheh *et al*. 2012) are calculated according to Eq. (7)

$$\begin{aligned} F_{el} &= \frac{1}{2}\varepsilon b_p(V_{DC}+V_{AC}\cos(\Omega t))^2\int_L^{L+2l_p}\frac{1}{(d-w_3(x))^2}dx\\ F_{fr} &= 0.325\varepsilon(V_{DC}+V_{AC}\cos(\Omega t))^2\int_L^{L+2l_p}\frac{1}{(d-w_3(x))}dx\\ M_{el} &= \frac{1}{2}\varepsilon b_p(V_{DC}+V_{AC}\cos(\Omega t))^2\int_L^{L+2l_p}\frac{(x-(L+L_p))}{(d-w_3(x))^2}dx\\ M_{fr} &= 0.325\varepsilon(V_{DC}+V_{AC}\cos(\Omega t))^2\int_L^{L+2l_p}\frac{(x-(L+L_p))}{(d-w_3(x))}dx \end{aligned} \tag{7}$$

Finally, the transverse displacement of rigid micro-plate, $w_3(x)$, can be written as follows

$$\begin{aligned} &w_3(x,t) = w_2(L,t) + l_p\theta + \left(x-\left(L+L_p\right)\right)\tan\theta\,,\\ &\theta = \frac{\partial w_2}{\partial x}|\hat{x}=\hat{l} \end{aligned} \tag{8}$$

By combining Eqs. (1), (6) and (7), the governing equation of motion, boundary and continuity conditions can be expressed as

$$\begin{aligned} &EI\frac{\partial^4 w_1}{\partial x^4} + \rho A\frac{\partial^2 w_1}{\partial t^2} + c\frac{\partial w_1}{\partial t} = 0, \quad 0\le x\le l_c\\ &EI\frac{\partial^4 w_2}{\partial x^4} + \rho A\frac{\partial^2 w_2}{\partial t^2} + c\frac{\partial w_2}{\partial t}\\ &= -\left[m_p\frac{\partial^2 w_2}{\partial t^2}|x=L\right]\delta(x-l)\\ &\quad +F_{el}\delta(x-l) + F_{fr}\delta(x-l)\\ &\quad -\left[\int_L^{L+2l_p} c\dot{w}_3\ dx\right]\delta(x-l)\\ &\quad +M_{el}\delta(x-l) + M_{fr}\delta(x-l)\\ &\quad -\left[I_p\frac{\partial^3 w_2}{\partial x\partial t^2}|x=l\right]\frac{\partial\delta(x-l)}{\partial x}\\ &\quad -\left[\int_L^{L+2l_p} c\left(x-l_p\right)\dot{w}_3\ dx\right]\frac{\partial\delta(x-l)}{\partial x}, \quad l_c\le x\le L \end{aligned} \tag{9}$$

For the convenience and the generalization of the findings, the following set of non-dimensional parameters are introduced

$$\begin{aligned} &\hat{x} = \frac{x}{l}, \quad \hat{w}_i = \frac{w_i}{d} \quad i = 1,2,3,\\ &\hat{t} = \frac{t}{T}T = \sqrt{\frac{\rho A l^4}{EI}}, \end{aligned} \tag{10}$$

Using the non-dimensional parameters described above, Eq. (9) is re-written as

$$
\begin{aligned}
&\frac{\partial^4 \widehat{w}_1}{\partial \hat{x}^4}+\frac{\partial^2 \widehat{w}_1}{\partial \hat{t}^2}+\hat{c}\frac{\partial \widehat{w}_1}{\partial \hat{t}}=0, \qquad 0\le \hat{x}\le \hat{l}_c,\\
&\frac{\partial^4 \widehat{w}_1}{\partial \hat{x}^4}+\frac{\partial^2 \widehat{w}_1}{\partial \hat{t}^2}+\hat{c}\frac{\partial \widehat{w}_1}{\partial \hat{t}}\\
&=-\alpha_3\left[\frac{\partial^2 \widehat{w}_2}{\partial \hat{t}^2}|\hat{x}=l\right]\delta(\hat{x}-\hat{l})+\alpha_{el}\left[(V_{DC}+V_{AC}\cos(\Omega t))^2\int_{\hat{l}}^{\hat{l}+2\hat{l}_p}\frac{1}{(1-\widehat{w}_3(\hat{x}))^2}d\hat{x}\right]\delta(\hat{x}-\hat{l})\\
&\quad+\alpha_{fr}\left[(V_{DC}+V_{AC}\cos(\Omega t))^2\int_{\hat{l}}^{\hat{l}+2\hat{l}_p}\frac{1}{(1-\widehat{w}_3(\hat{x}))}d\hat{x}\right]\delta(\hat{x}-\hat{l})-\left[\int_{\hat{l}}^{\hat{l}+2\hat{l}_p}\hat{c}\widehat{w}_3\ d\hat{x}\right]\delta(\hat{x}-\hat{l})\\
&\quad-\alpha_4\left[\frac{\partial^3 \widehat{w}_2}{\partial \hat{x}\partial \hat{t}^2}|\hat{x}=l\right]\frac{\partial\delta(\hat{x}-\hat{l})}{\partial\hat{x}}+\alpha_{el}\left[(V_{DC}+V_{AC}\cos(\Omega t))^2\int_{\hat{l}}^{\hat{l}+2\hat{l}_p}\frac{\left(\hat{x}-(\hat{l}+\hat{l}_p)\right)}{(1-\widehat{w}_3(\hat{x}))^2}d\hat{x}\right]\frac{\partial\delta(\hat{x}-\hat{l})}{\partial\hat{x}}\\
&\quad+\alpha_{fr}\left[{V_{DC}}^2\int_{\hat{l}}^{\hat{l}+2\hat{l}_p}\frac{\left(\hat{x}-(\hat{l}+\hat{l}_p)\right)}{(1-\widehat{w}_3(\hat{x}))}d\hat{x}\right]\frac{\partial\delta(\hat{x}-\hat{l})}{\partial\hat{x}}-\left[\int_{\hat{l}}^{\hat{l}+2\hat{l}_p}\hat{c}(\hat{x}-\hat{l}_c)\widehat{w}_3\ d\hat{x}\right]\frac{\partial\delta(\hat{x}-\hat{l})}{\partial\hat{x}}, \qquad \hat{l}_c\le\hat{x}\le\hat{l},\\
&\widehat{w}_1|\hat{x}=0=0, \qquad \frac{\partial\widehat{w}_1}{\partial\hat{x}}|\hat{x}=0=0, \qquad \frac{\partial^2\widehat{w}_2}{\partial\hat{x}^2}|\hat{x}=l=0,\\
&\frac{\partial^3\widehat{w}_2}{\partial\hat{x}^3}|\hat{x}=l=0, \quad \widehat{w}_1|x=l_c=\widehat{w}_2|x=l_c\\
&\frac{\partial^2\widehat{w}_1}{\partial x^2}|x=l_c=\frac{\partial^2\widehat{w}_2}{\partial x^2}|x=l_c, \qquad \frac{\partial^3\widehat{w}_1}{\partial x^3}|x=l_c=\frac{\partial^3\widehat{w}_2}{\partial x^3}|x=l_c\\
&\frac{\partial^2\widehat{w}_2}{\partial x^2}|x=l_c=\widehat{K}_\theta\left(\frac{\partial^2 w_2}{\partial x^2}|x=l_c-\frac{\partial^2\widehat{w}_2}{\partial x^2}|x=l_c\right)
\end{aligned}
\tag{11}
$$

where

$$
\widehat{K}_\theta=\frac{K_\theta L}{EI}, \quad \alpha_{el}=\frac{\varepsilon b_p l^4}{2EId^3}, \quad \alpha_{fr}=\frac{0.325\varepsilon l^4}{EId^3}, \quad \alpha_3=\frac{m_T}{\rho A}, \quad \alpha_4=\frac{I_T}{\rho Al}, \quad \hat{c}=\frac{cd}{\sqrt{\frac{\rho Al^4}{EI}}} \tag{12}
$$

The equivalent force and moment terms from Eq. (11) are moved to the boundary conditions for the free end of the beam. Finally, the following equations of motion, boundary and continuity conditions are obtained

$$
\begin{aligned}
&\frac{\partial^4\widehat{w}_1}{\partial x^4}+\frac{\partial^2\widehat{w}_1}{\partial t^2}=0 \qquad 0\le x\le\hat{l}_c\\
&\frac{\partial^4\widehat{w}_2}{\partial x^4}+\frac{\partial^2\widehat{w}_2}{\partial t^2}=0 \qquad \hat{l}_c\le x\le 1
\end{aligned}
\tag{13}
$$

$$
\begin{aligned}
&\frac{\partial^3\widehat{w}_2(\hat{l},\hat{t})}{\partial\hat{x}^3}+\alpha_{el}(V_{DC}+V_{AC}\cos(\Omega t))^2\int_{\hat{l}}^{\hat{l}+2\hat{l}_p}\frac{1}{(1-\widehat{w}_2(x,t))^2}d\hat{x}\\
&+\alpha_{fr}(V_{DC}+V_{AC}\cos(\Omega t))^2\int_{\hat{l}}^{\hat{l}+2\hat{l}_p}\frac{1}{1-\widehat{w}_2(x,t)}d\hat{x}=\hat{m}_p\frac{\partial^2\widehat{w}_3(\hat{l}_1,\hat{t})}{\partial\hat{t}^2},\\
&-\frac{\partial^2\widehat{w}_2(\hat{l},\hat{t})}{\partial\hat{x}^2}-\left[\frac{\partial^3\widehat{w}_2(\hat{l},\hat{t})}{\partial\hat{x}^3}\right]\hat{l}_p+\alpha_{el}(V_{DC}+V_{AC}\cos(\Omega t))^2\int_{\hat{l}}^{\hat{l}+2\hat{l}_p}\frac{\left(\hat{x}-(\hat{l}+\hat{l}_p)\right)}{(1-\widehat{w}_3(x))^2}d\hat{x}\\
&+\alpha_{fr}(V_{DC}+V_{AC}\cos(\Omega t))^2\int_{\hat{l}}^{\hat{l}+2\hat{l}_p}\frac{(\hat{x}-(\hat{l}+\hat{l}_p))}{1-\widehat{w}_3(x)}d\hat{x}=\hat{I}_p\times\frac{\partial^2\hat{\theta}}{\partial\hat{t}^2}\\
&\widehat{w}_1|x=0=0,\frac{\partial\widehat{w}_1}{\partial x}|x=0=0, \qquad \widehat{w}_1|x=l_c=\widehat{w}_2|x=l_c,\\
&\frac{\partial^2\widehat{w}_1}{\partial x^2}|x=l_c=\frac{\partial^2\widehat{w}_2}{\partial x^2}|x=l_c, \qquad \frac{\partial^3\widehat{w}_1}{\partial x^3}|x=l_c=\frac{\partial^3\widehat{w}_2}{\partial x^3}|x=l_c,\\
&\frac{\partial^2\widehat{w}_2}{\partial x^2}|x=l_c=\widehat{K}_\theta\left(\frac{\partial^2 w_2}{\partial x^2}|x=l_c-\frac{\partial^2\widehat{w}_2}{\partial x^2}|x=l_c\right)
\end{aligned}
\tag{14}
$$

2.1 Static deflection and natural frequency

The static equilibrium equations, presented in Eq. (15), are obtained by setting the terms involving the time derivatives to zero.

$$
\begin{aligned}
&\frac{\partial^4 w_{s1}}{\partial x^4}=0 \qquad 0\le x\le l_c\\
&\frac{\partial^4 w_{s2}}{\partial x^4}=0 \qquad l_c\le x\le L
\end{aligned}
\tag{15}
$$

Similarly, the boundary and continuity conditions are shown in Eq. (16).

$$
\begin{aligned}
&w_{s1}|x=0=0, \qquad \frac{\partial w_{s1}}{\partial x}|x=0=0\\
&-\frac{\partial^2 w_{s2}}{\partial x^2}|x=L+\alpha_{el}(V_{DC})^2\int_L^{L+l_p}\frac{(x-(\hat{l}+\hat{l}_p))}{(1-w_{s3}(x))^2}dx+\alpha_{fr}(V_{DC})^2\int_L^{L+l_p}\frac{(x-(\hat{l}+\hat{l}_p))}{(1-w_{sp}(x))}dx=0\\
&\frac{\partial^3 w_{s2}}{\partial x^3}|x=l+\alpha_{el}(V_{DC})^2\int_L^{L+l_p}\frac{1}{(1-w_{s3}(x))^2}dx+\alpha_{fr}(V_{DC})^2\int_L^{L+l_p}\frac{1}{(1-w_{s3}(x))}dx=0
\end{aligned}
\tag{16}
$$

The final form of the static deflection, $w_{s3}(x)$, is given in Eq. (17)

$$
\begin{aligned}
&w_{s3}(x)=w_{s2}(L)+\frac{l_p}{2}\frac{\partial w_{s2}}{\partial x}|\hat{x}=\hat{l}+(x-(L+\frac{l_p}{2}))\frac{\partial w_{s2}}{\partial x}|\hat{x}=\hat{l}\\
&w_{s1}|x=l_c=w_{s2}|x=l_c, \qquad \frac{\partial^2 w_{s1}}{\partial x^2}|x=l_c=\frac{\partial^2 w_{s2}}{\partial x^2}|x=l_c, \qquad \frac{\partial^3 w_{s1}}{\partial x^3}|x=l_c=\frac{\partial^3 w_{s2}}{\partial x^3}|x=l_c\\
&EI\frac{\partial^2 w_{s2}}{\partial x^2}|x=l_c=K_\theta\left(\frac{\partial w_{s2}}{\partial x}|x=l_c-\frac{\partial w_{s1}}{\partial x}|x=l_c\right)
\end{aligned}
\tag{17}
$$

The general solution of Eq. (15) can be obtained as

$$
\begin{aligned}
&\frac{\partial^4 \hat{w}_{s1}}{\partial \hat{x}^4}=0\Rightarrow \hat{w}_{s1}(\hat{x})=A_1\hat{x}^3+A_2\hat{x}^2+A_3\hat{x}+A_4,\\
&\frac{\partial^4 \hat{w}_{s2}}{\partial \hat{x}^4}=0\Rightarrow \hat{w}_{s2}(\hat{x})=A_5\hat{x}^3+A_6\hat{x}^2+A_7\hat{x}+A_8,
\end{aligned}
\tag{18}
$$

where $A_i,\ i=1..8$ are unknown coefficients, which are calculated by considering the boundary conditions and continuity equations defined in Eqs. (16) and (17), respectively. The microbeam deflection is the summation of the static, $w_{si}(x)$, and dynamic solutions $u_i(x,t),\ i=1,2,3$ as given in Eq. (19)

$$
\hat{\boldsymbol{w}}_{\boldsymbol{i}}(\hat{\boldsymbol{x}},\hat{\boldsymbol{t}})=\hat{\boldsymbol{w}}_{\boldsymbol{Si}}(\hat{\boldsymbol{x}})+\boldsymbol{u}_{\boldsymbol{i}}(\hat{\boldsymbol{x}},\hat{\boldsymbol{t}}),\quad \boldsymbol{i}=\mathbf{1},\mathbf{2},\mathbf{3} \tag{19}
$$

As the next step, Eq. (19) is substituted in Eqs. (13) and (14), in which the Taylor series expansion of the electrical force about $u_3(x,t)$ is used. Then, by employing Eqs. (16) and (17), the terms that represent equilibrium position are eliminated. The resulting equations of motion about static deflection and associated boundary conditions are given in Eq. (20)

$$
\begin{aligned}
&\frac{\partial^4 u_1}{\partial \hat{x}^4}+\frac{\partial^2 u_1}{\partial \hat{t}^2}=0, \qquad 0\le\hat{x}\le\hat{l}_c\\
&\frac{\partial^4 u_2}{\partial \hat{x}^4}+\frac{\partial^2 u_2}{\partial \hat{t}^2}=0, \qquad \hat{l}_c\le\hat{x}\le 1\\
&u_1(0,\hat{t})=0, \qquad \frac{\partial u_1}{\partial \hat{x}}(0,\hat{t})=0\\
&\frac{\partial^3 u_2(\hat{l}_1,\hat{t})}{\partial \hat{x}^3}+\alpha_{el}\left(V_{DC}+V_{AC}\cos(\hat{\Omega}\hat{t})\right)^2\int_L^{L+2l_p}\frac{u_3(\hat{x},\hat{t})}{(1-\hat{w}_{S3}(\hat{x}))^3}d\hat{x}\\
&\quad+\alpha_{fr}\left(V_{DC}+V_{AC}\cos(\hat{\Omega}\hat{t})\right)^2\int_L^{L+2l_p}\frac{1}{(1-\hat{w}_{S3}(\hat{x}))^2}d\hat{x}=\hat{m}_p\frac{\partial^2 u_3}{\partial \hat{t}^2}\\
&-\frac{\partial^2 u_2(\hat{l}_1,\hat{t})}{\partial \hat{x}^2}+\alpha_{el}\left(V_{DC}+V_{AC}\cos(\hat{\Omega}\hat{t})\right)^2\int_L^{L+2l_p}\frac{\left(x-(\hat{l}+\hat{l}_p)\right)\times u_3(\hat{x})}{(1-\hat{w}_{S3}(\hat{x}))^3}d\hat{x}\\
&\quad+\alpha_{fr}\left(V_{DC}+V_{AC}\cos(\hat{\Omega}\hat{t})\right)^2\int_L^{L+2l_p}\frac{\left(x-(\hat{l}+\hat{l}_p)\right)}{(1-\hat{w}_{S3}(\hat{x}))^2}d\hat{x}=\hat{I}_p\frac{\partial^3 u_2(\hat{l}_1,\hat{t})}{\partial\hat{x}\partial\hat{t}^2}
\end{aligned}
\tag{20}
$$

The natural frequencies and corresponding mode shapes about the static equilibrium position are obtained by simply substituting $u_i(\hat{x},\hat{t})=\varphi_i(\hat{x})e^{i\omega\hat{t}},i=1,2,3$ into Eq. (20). By substituting Eq. (19) into Eq. (14), expanding the forces and electrostatic moments around static equilibrium position up to third order, and removing the pure static terms, the nonlinear equation of motion about static position is finalized (see Appendix 1 for the details). Then, this equation is discretized using the Galerkin method. For that purpose, it is assumed that $\hat{u}_i(\hat{x},\hat{t})=p(t)\times\varphi_i\ i=1,2,3$, where φ_1,φ_2 and $\varphi_3$are functions of linear mode shapes of vibration about static equilibrium position along the length of the section 1 and 2 of the microbeam and proof mass, respectively. Similarly, $p(t)$ is the time domain response of the system. By substituting this assumption into equation (available in Appendix 1) and summing two equations of systems can be stated as

$$
\begin{aligned}
&M_1p(t)+M_2p^2(t)+M_3p^3(t)+M_4\dot{p}(t)+M_5\ddot{p}(t)\\
&+M_6V_{ac}\cos(\Omega t)+M_7{V_{ac}}^2\cos^2(\Omega t)\\
&+M_8V_{ac}p(t)\cos(\Omega t)=0
\end{aligned}
\tag{21}
$$

where the coefficient of $M_i,i=1..8$ are described in Appendix 2. Eq. (21) is solved by analytical multiple scale perturbation method, which is explained in the next section.

2.2 Multiple scale perturbation method

Eq. (21) can be solved using multiple scale method of perturbation theory assuming that the nonlinear terms have lower orders compared to the linear terms. Therefore, $p(t)$ can be represented as in Eq. (22)

$$p(t) = \varepsilon\ p_1(T_0,T_1,T_2) + \varepsilon^2\ p_2(T_0,T_1,T_2) + \varepsilon^3\ p_3(T_0,T_1,T_2) \tag{22}$$

where $T_0 = t,\ \ T_1 = \varepsilon\ t,\ \ T_2 = \varepsilon^2\ t$, are time scales and ε is a dimensionless book-keeping parameter, which represents the order of the expressions. The derivatives of these functions, shown in Eq. (23), are calculated using the chain rule

$$\begin{aligned}\frac{\partial}{\partial t} &= \frac{\partial}{\partial T_0} + \varepsilon\frac{\partial}{\partial T_1} + \varepsilon^2\frac{\partial}{\partial T_2}\\ \frac{\partial}{\partial t^2} &= \frac{\partial}{\partial T_0}^2 + 2\varepsilon\frac{\partial}{\partial T_0}\frac{\partial}{\partial T_1} + \varepsilon^2\frac{\partial}{\partial T_1}^2 + 2\varepsilon^2\frac{\partial}{\partial T_0}\frac{\partial}{\partial T_2}\end{aligned} \tag{23}$$

In order to balance the nonlinear terms with the terms of air damping and excitation, these terms are considered as order ε^2 and ε^3, respectively. By this assumption and substituting Eqs. (22) and (23) into Eq. (21), Eqs. (26) to (28) are obtained. In this derivation, the equations with the same power of ε are collected. Ordering ε^1 terms yield Eq. (24)

$$\frac{\partial^2 p_1(T_0,T_1,T_2)}{\partial T_0^2} + N_1 p_1(T_0,T_1,T_2) = 0, \quad N_1 = \frac{M_1}{M_5} \tag{24}$$

Similarly, ordering ε^2 terms yield Eq. (25)

$$\begin{aligned}&\frac{\partial^2 p_2(T_0,T_1,T_2)}{\partial T_0^2} + N_1 p_2(T_0,T_1,T_2)\\ &= -2\frac{\partial^2 p_1(T_0,T_1,T_2)}{\partial T_0 \partial T_1} - N_2 p_1(T_0,T_1,T_2)^2,\\ &N_2 = \frac{M_2}{M_5}\end{aligned} \tag{25}$$

Finally, ε^3 terms are collected as shown in Eq. (26)

$$\begin{aligned}&\frac{\partial^2 p_3(T_0,T_1,T_2)}{\partial T_0^2} + N_1 p_3(T_0,T_1,T_2)\\ &= -2\frac{\partial^2 p_1(T_0,T_1,T_2)}{\partial T_0 \partial T_2} - 2\frac{\partial^2 p_2(T_0,T_1,T_2)}{\partial T_0 \partial T_1} - \frac{\partial^2 p_1}{\partial T_1^2}\\ &\quad -2N_2 p_1(T_0,T_1,T_2) p_2(T_0,T_1,T_2)\\ &\quad -N_3\frac{\partial p_1(T_0,T_1,T_2)}{\partial T_0} - N_4 p_1(T_0,T_1,T_2)^3\\ &\quad -N_6\ V_{AC}\cos(\Omega T_0) - N_7 V_{AC}^2\cos^2(\Omega T_0),\\ &N_3 = \frac{M_3}{M_5} \quad N_4 = \frac{M_4}{M_5} \quad N_6 = \frac{M_6}{M_5} \quad N_7 = \frac{M_7}{M_5}\end{aligned} \tag{26}$$

Since $\omega = \sqrt{N_1}$, the homogeneous solution of Eq. (25) is as follows

$$p_1 = A(T_1,T_2)e^{i\omega T_0} + \bar{A}(T_1,T_2)e^{-i\omega T_0} \tag{27}$$

where $A(T_1,T_2)$ is a complex constant. By substituting Eq. (27) into Eq. (24)

$$\begin{aligned}&\frac{\partial^2 p_2}{\partial T_0^2} + N_1 p_2\\ &= \left(-2i\omega\frac{\partial A}{\partial T_1}\right)e^{i\omega T_0} + (N_2 A^2)e^{2i\omega T_0} + N_2 A\bar{A} + C_c\end{aligned} \tag{28}$$

where C_c stands for the complex conjugate of the preceding terms. Eliminating the secular terms from p_2 requires that $A = B(T_2)$. The particular solution of Eq. (28) is given as

$$p_2 = \frac{N_2}{3\omega^2}A^2 e^{2i\omega T_0} + \frac{N_2}{3\omega^2}\bar{A}^2 e^{-2i\omega T_0} - 2\frac{N_2}{\omega^2}A\bar{A} \tag{29}$$

By substituting p_1 and p_2 from Eq. (27) and Eq. (29), into Eq. (26), considering resonance frequency as $\Omega = \omega + \varepsilon^2\sigma$, and keeping the terms that contain secular terms, Eq. (30) is obtained

$$\begin{aligned}&\frac{\partial^2 p_3}{\partial T_0^2} + N_1 p_3\\ &= \left(-i\omega N_4 A - 2i\omega A' + N_5 A^2\bar{A} + \frac{N_6}{2}e^{i\sigma T_2}\right)e^{i\omega T_0}\\ &\quad + C_c + NST\\ &N_5 = \frac{10N_2^2}{3\omega^2} - 3N_3\end{aligned} \tag{30}$$

where σ is the detuning parameter, and NST represents the rest of the terms, which do not produce secular terms. By expressing A in the polar form ($A = \frac{1}{2}a(T_2)e^{i\beta}$) and substituting it into Eq. (30), elimination of secular terms requires

$$\begin{aligned}&-ia' + a\beta' + \frac{1}{8}N_5 a^3 - \frac{1}{2}N_4 i\omega a + \frac{N_6}{2}\cos(\sigma T_2 - \beta)\\ &+i\frac{N_6}{2}\sin(\sigma T_2 - \beta) = 0\end{aligned} \tag{31}$$

Assuming $\gamma = \sigma T_2 - \beta$, and separating real and imaginary parts in Eq. (31) yields

$$a' = -\frac{1}{2}N_4 a + \frac{N_6}{2\omega}\sin\gamma \tag{32}$$

$$a\gamma' = \sigma a + \frac{1}{8\omega}N_5 a^3 + \frac{N_6}{2\omega}\cos\gamma \tag{33}$$

By letting a' and $\gamma'$to be equal to the zero in the Eq. (32) and Eq. (33), the equilibrium point can be obtained as follows

$$\frac{1}{2}N_4\omega a = \frac{N_6}{2}\sin\gamma \tag{34}$$

$$\left(\sigma\omega + \frac{1}{8}N_5 a^2\right)a = -\frac{N_6}{2}\cos\gamma \tag{35}$$

By squaring Eqs. (34) and (35) and adding them up, the frequency response equation is obtained as follows

$$\frac{1}{4}{N_4}^2\omega^2a^2+\left(\sigma\omega+\frac{1}{8}N_5a^2\right)^2a^2={\frac{N_6}{4}}^2 \quad (36)$$

3. Effect of crack on the pull-in instability

The effect of cracks in the static and dynamic pull-in instability in MEMS applications is well known in the literature (Zhou *et al*. 2015, Motallebi *et al*. 2012, Hassannejad and Amiri Jahed 2018, Akbas 2018, Al-Basyouni *et al*. 2015, Dastjerdi and Abbasi 2019, Shaat *et al*. 2016). Therefore, we investigate the effect of crack parameters such as the position and depth of the cracks on the static and dynamic pull-in in this section. The physical and geometrical properties of the gas sensor are presented in Table 3.

Table 3 Geometric and physical parameters of the gas sensor

L	b	h	L_p	b_p	h_p
250 µm	5 µm	1.5 µm	25 µm	20 µm	2 µm
E	ρ	ε	d	V_{DC}	V_{AC}
160 Gpa	2300 kg/m^3	8.854×10^{-12} F/m	4 µm	6 v	0.1 v

3.1 The effect of crack on the static pull-in of system

If a voltage is applied between the rigid plate and the electrode, the electrostatic force deflects the micro-cantilever beam to a new static position. When the voltage exceeds a critical value, the mechanical restoring force of the microbeam can no longer maintain the opposing electrostatic force leading to the collapse of the structure. This voltage is known as static pull-in voltage, which is independent of time or primary location of the microbeam (Younis 2011). The maximum deflection of micro-cantilever beam as a function of VDC is plotted in Fig. 4. The parameters are taken from the literature (Nayfeh *et al*. 2010). In the analysis, the crack and fringing field effects are not taken into account. The results are in good agreement with the previous study from the literature (Nayfeh *et al*. 2010).

The maximum static deflection versus the applied DC voltage for different crack length and depth is shown in Fig. 5. The results show that, the pull-in occurs earlier when there is a crack in the microsystem due to the fact that crack increases the local flexibility of the microbeam. The results yield that the pull-in voltage has the lowest magnitude at the fixed end of microcantilever, i.e., Lc = 0, while it increases when the crack is closer to the microbeam's free end. Furthermore, it can be observed that by increasing the depth

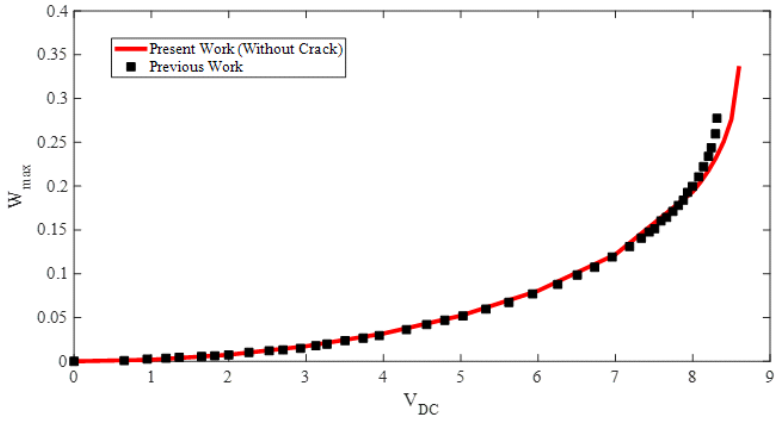

Fig. 4 Maximum deflection of micro-cantilever beam as a function of V_{DC}

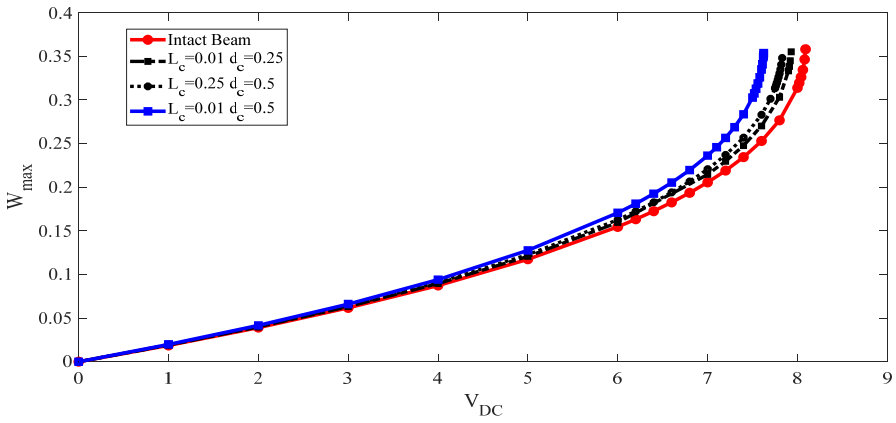

Fig. 5 Maximum deflection of micro-cantilever beam as a function of V_{DC} for cracks with different length and depth

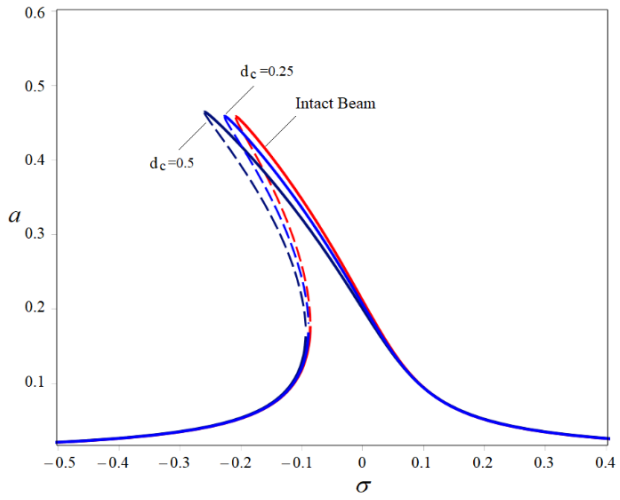

Fig. 6 The variation of response amplitude *a* with respect to σ for different values of the crack depth

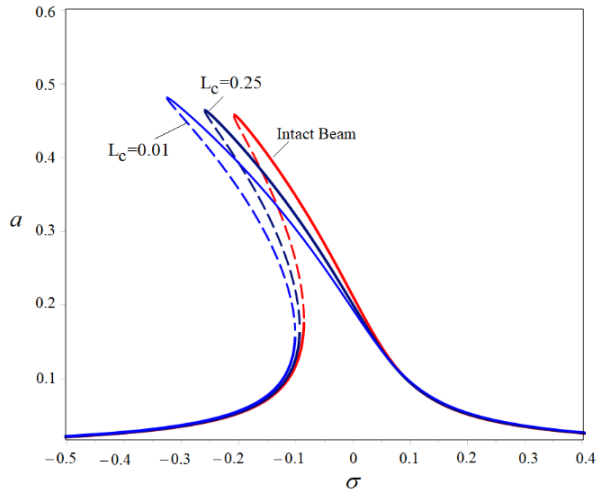

Fig. 7 The variation of response amplitude *a* with respect to σ for different values of the crack length

Table 4 The first four natural frequencies of the intact beam

f_1 (Hz)	f_2 (Hz)	f_3 (Hz)	f_4 (Hz)
1.3416	13.1624	39.5280	80.5635

of the crack the static pull-in voltage decreases. The results from Fig. 5 show that for the lower voltage effect of crack length is negligible.

3.2 The effect of crack on the dynamic pull-in of system

When the rate of change in the voltage is not negligible, the inertia effects should be taken into consideration in the dynamic analysis of the microsystem. Under these conditions, the pull-in instability is called the dynamic pull-in and the voltage that causes the instability is called dynamic pull-in voltage. Another important phenomenon in the electrostatically actuated microbeams is the shift of resonance frequency due to the nonlinearities of the systems. This condition occurs when the AC and DC voltages are applied between microbeam and electrode simultaneously. The changes of the system's equilibrium amplitude *a* versus the change of σ at the primary resonances for different values of nondimensional crack depth and length are plotted in Figs. 7 and 8, respectively. These results show the softening behavior as a result of the softening nature of the electrostatic force. Moreover, it can be observed that the presence of crack increases with the nonlinear shift of the resonance frequency as well as the maximum amplitude. Fig. 5 indicates the influence of crack depth on the resonance frequency. The nonlinear shift of resonance frequency for a system with L_c = 0.25 may be further decreased by decreasing the value of nondimensional depth without a main change on the value of the amplitude at the resonance peak. Fig. 6 demonstrates that both the nonlinear shift of the resonance frequency and the maximum amplitude increase when the crack is located closer to the fixed end of the microcantilever.

4. The effect of crack on natural frequencies

To evaluate the effect of crack on the natural frequency, the natural frequencies of the cracked microbeam with tip mass under electrostatic actuation are calculated according to the methodology outlined in Section 2.1. The first four bending natural frequencies are plotted in Fig. 8 as a function of crack depth and location. The first four bending natural frequencies are summarized in Table 4. The results show that the natural frequency decreases with the increased crack depth. Furthermore, it can be concluded from Fig. 8 that changing the crack depth is more influential in the higher frequencies. For example, the rate of change in the fourth natural frequency is comparably higher than the first natural frequency when the non-dimensional crack depth changes from 0.1 to 0.2. To investigate the effect of the crack parameters on natural frequency, 12 cases with different crack parameters are chosen. The natural frequencies corresponding to these cases are summarized in Table 5.

Table 5 Results for the first four bending natural frequencies

TN	L_c	D_c	f_1 (Hz)	f_2 (Hz)	f_3 (Hz)	f_4 (Hz)
1	0.2	0.1	1.3387	13.1618	39.5060	80.4468
2	0.2	0.15	1.3368	13.1616	39.4888	80.3546
3	0.2	0.2	1.3358	13.1615	39.4801	80.3076
4	0.4	0.1	1.3402	13.1460	39.4966	80.5331
5	0.4	0.15	1.3394	13.1332	39.4720	80.5093
6	0.4	0.2	1.3390	13.1267	39.4594	80.4971
7	0.6	0.1	1.3410	13.1404	39.4894	80.5351
8	0.6	0.15	1.3408	13.1233	39.4591	80.5129
9	0.6	0.2	1.3407	13.1145	39.4436	80.5015
10	0.8	0.1	1.3412	13.1578	39.4769	80.4031
11	0.8	0.15	1.3412	13.1545	39.4364	80.2763
12	0.8	0.2	1.3412	13.1527	39.4156	80.2116

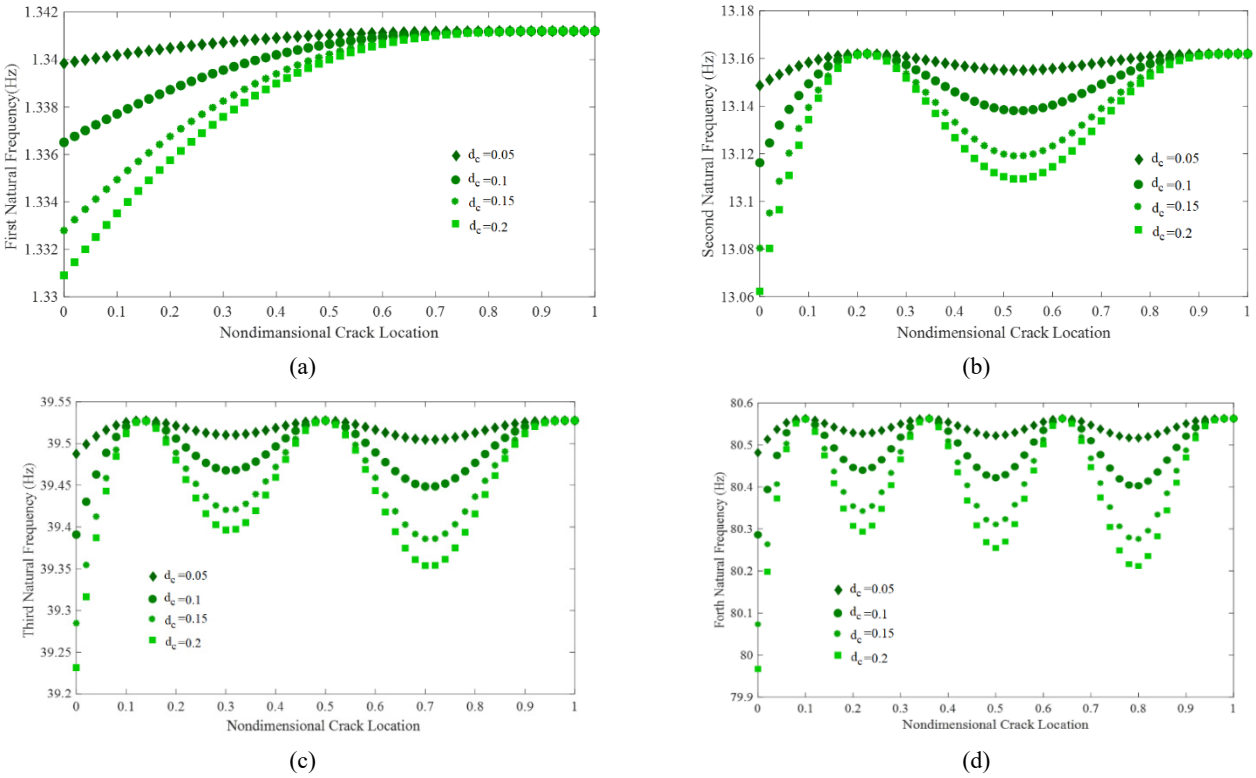

Fig. 8 Natural frequency of microsystem with an open-edge crack versus the location for different crack depth (a) 1st natural frequency; (b) 2nd natural frequency; (c) 3rd natural frequency; and (d) 4th natural frequency

5. Crack detection using optimization methods

It has been shown in Section 4 that the parameters of the depth and location of the crack lead to a change in natural frequencies compared to the original structure without any cracks. Therefore, this knowledge can be used to determine the location and depth of possible cracks using optimization methods. Towards this end, the objective function, given in Eq. (37), is considered as the weighted squared difference between the measured and calculated natural frequencies. Furthermore, the depth and location of the crack are considered as the optimization design variables. The depth of the crack varies from 0 and the height of the micro-cantilever beam, while the location of the crack ranges from 0 mm and the length of the micro-cantilever beam. These constraints are expressed in Eq. (38).

$$Cost(l_c, d_c) = \sum_{i=1}^{4} \Phi_i (f_i - f_i^*)^2 \qquad (i = 1,2,3,4) \qquad (37)$$

subjected to

$$0 < d_c < h, \qquad 0 < l_c < L \qquad (38)$$

where Φ_i is the i^{th} weighting factor. f_i and f_i^* are the i^{th} measured natural frequency of the cracked micro-cantilever beam, and the i^{th} natural frequency estimated from the optimization algorithm, respectively. Since the change in higher natural frequencies are more than the lower frequencies, a weighting factor is introduced for each mode with a scale factor, $\frac{1}{i}$ (Casciati 2008), in order to account for the effect of each mode equally.

6. Methodology

In this section, the methodology to solve the optimization problem defined in Section 5 is presented. Since proposed methodology is based on the HHO algorithm, this algorithm is briefly described in Section 6.1. Then the proposed hybrid algorithm is explained in Section 6.2. The parameters of the algorithm are tuned using the Taguchi Design method to compare the results fairly with the algorithms in the literature. Taguchi Design method is briefly presented in Section 6.3.

6.1 Harris Hawk Optimization Algorithm (HHO)

Harris Hawk Optimization (HHO) algorithm is inspired by the cooperative behavior of Harris Hawks in chasing the prey (Heidari *et al*. 2019). The ability of Harris Hawks to attack in different directions at the same time and their attempt to surprise the prey from various paths have been the building block of the algorithm. Three stages of the HHO algorithm are as follow: 1) the first stage is the exploration stage, in which new and variable responses are generated, 2) the transition from exploration to exploitation is performed based on the external energy of the prey, and 3) finally, local improvement of the responses from the exploration stage is carried out. The exploration stage can be formed as follows

$$x(t+1)=\begin{cases}x_{rand}(t)-r_1|x_{rand}(t)-2r_2x(t)| & q\geq 0\\ x_{prey}(t)-x_m(t)-r_3\big(LB+r_4(UB-LB)\big) & q\prec 0\end{cases} \quad (39)$$

where $x(t)$ and $x(t+1)$ are the current location and the location of the Harris Hawk in the next iteration t, respectively. $X_{prey}(t)$ is the location of prey, r_1, r_2, r_3, r_4 and q are arbitrary numbers between zero and one. $X_{rand}(t)$ is the randomly selected hawk from the population. Moreover, LB and UB indicate the lower and upper limits of variables, respectively. $X_m(t)$ is the average position of Harris Hawks, which can be determined according to Eq. (40).

$$x_m(t)=\frac{1}{N}\sum_{i=1}^{N}x_i(t) \quad (40)$$

where *N* is the number of all Harris Hawks and illustrates the position of each Harris Hawk for iteration corresponding to time *t*. Apparently, the energy of the hawks is lessened during chasing and hunting, which is represented by Eq. (41)

$$E=2E_0\left(1-\frac{t}{T}\right) \quad (41)$$

E denotes the escaping energy, E_0 stands for the initial energy, and T indicates the maximum number of iterations. In this stage, the value of E_0 determines the phase: $|E_0|\geq 1$ represents the exploration phase, and $|E_0|\prec 1$ corresponds to the exploitation phase. The hawks' surprising attack to the prey is performed from the previous phase in the exploitation phase. There are four models to represent the exploitation phase:

- Soft surround: $r\geq 0$ and $|E|\geq 0$, which can be calculated as

$$x(t+1)=\Delta x(t)-E\left|Jx_{prey}(t)-2x(t)\right| \quad (42)$$

$$\Delta x(t)=x_{prey}(t)-x(t) \quad (43)$$

where Δx is the difference between the prey location and the current location of Hawk corresponding to iteration at time, *t*. *J* is the random jump severity of the prey, which can be stated as follows

$$J=2(1-r_5) \quad (44)$$

where r_5 is a random number in the interval (0,1).

- Hard surround: $r\geq 0$ and $|E|\prec 0$.

In this stage, the prey is tired and does not have enough energy to escape. This phase is modeled as follows

$$x(t+1)=x_{prey}(t)-E_n|\Delta x(t)| \quad (45)$$

- Soft surround with progressive rapid dive: $r\prec 0$ and$|E|\geq 0$

In this phase, the prey has sufficient energy to escape successfully. In this step, hawk examines the next move for performing soft surround that can be obtained as

$$x=x_{prey}(t)-E\left|Jx_{prey}(t)-x(t)\right| \quad (46)$$

$$Z=Y+S+LF(D) \quad (47)$$

where D indicates the dimension and S is a random vector by size$1\times D$ and LF is the levy flight function (Heidari *et al*. 2019, Yang 2010). This can be represented as follows:

$$x(t+1)=\begin{cases}Y & f(Y)\prec f(y(t))\\ Z & f(Z)\prec f(y(t))\end{cases} \quad (48)$$

- Hard surround with progressive: $r\prec 0$ and$|E|\prec 0$.

The prey in this case does not have sufficient energy in order to escape properly, which can be expressed as follows

$$x(t+1)=\begin{cases}x_{prey}(t)-E\left|Jx_{prey}(t)-x_m(t)\right| & f(Y)\prec f(y(t))\\ Z=Y+S+LF(D) & f(Z)\prec f(y(t))\end{cases} \quad (49)$$

6.2 Proposed hybrid algorithm based on Nelder-Mead (HHO-NM)

The Nelder-Mead (N-M) simplex search method (Nelder and Mead 1965) is a local search method for solving unconstrained optimum problems without using gradient information. N-M algorithm is effective in finding improved solution and shows superiority compared to the algorithms based on random search. Furthermore, the N-M algorithm makes it possible to re-scale or reshape due to simplex search by considering the local behavior of the response function. In addition, the search direction in N-M algorithm is determined from the comparison of the function values, which are insensitive to small inaccuracies. However, this algorithm is very sensitive to the selection of initial points and there is no guarantee for finding the global optimum (Sarakhsi *et al*. 2016).

The hybrid algorithms are used previously in the literature (Vakil-Baghmisheh *et al*. 2012, Yildiz *et al*. 2019b, Ma *et al*. 2020, Sarakhsi *et al*. 2016, Rajan and Malakar 2015, Ye *et al*. 2020a, b) to achieve a better exploration and exploitation. Previous research (Vakil-Baghmisheh *et al*. 2012, Yildiz *et al*. 2019b, Sarakhsi *et al*. 2016, Rajan and Malakar 2015) indicate that hybrid algorithms based on N-M can overcome the slow convergence rate and trapping in the local optima. Therefore, it is possible to find the optimum solution with a lower number of function evaluations. In this paper the three novel algorithms are combined with N-M to improve the convergence and accuracy for obtaining the optimal solution. The flowchart of the proposed hybrid algorithms is demonstrated in Fig. 9. There are three main steps in the proposed hybrid algorithms: 1) The first optimization algorithm (HHO) predicts the location and depth of the

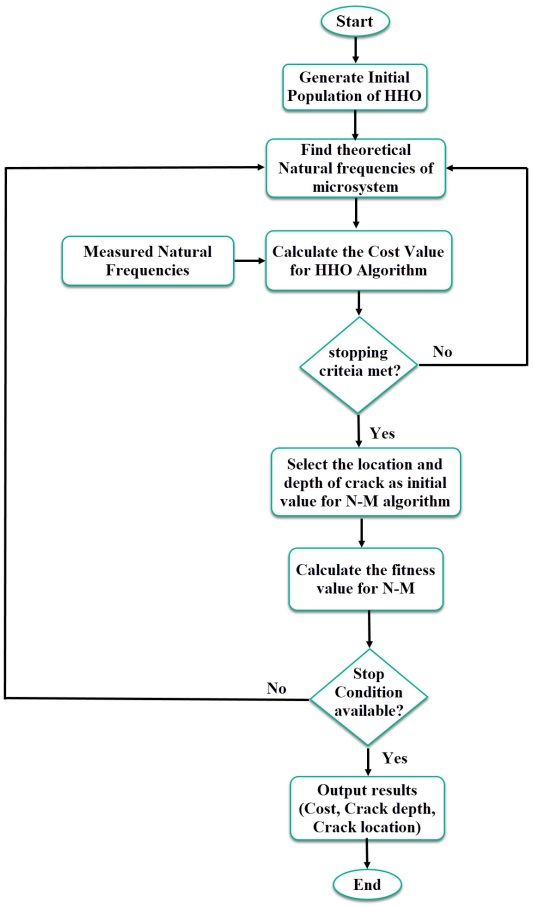

Fig. 9 Flowchart of proposed hybrid algorithm

crack, 2) the results from first step are taken as the initial values for the N-M optimization method, and 3) The N-M algorithm is applied to the beam with an open-edge crack to find the location and depth of the crack as the optimization design variables.

6.2 Taguchi Design of Experiment (DOE) Method

This section describes the details of the Taguchi design of experiment to tune the optimization algorithm parameters. The Taguchi method is an experimental design method that provides a systematic procedure to tune the parameters of the optimization algorithms. Taguchi DOE method can be used to reduce the number of experiments by employing orthogonal arrays and reducing the effects out of control factors. The essence of the Taguchi design of experiment method is to minimize the variance of the signal to noise ratio (S/N), which is regarded as the objective function. In this method, orthogonal arrays (OA) are utilized to reduce the number of experiment, which would lead to a reduction in computational time. In the present study, the L25 array of Taguchi design of experiment method is employed. The Taguchi method performs a sensitivity analysis to select a proper level for each parameter. The Signal-to-noise (S/N) ratio as the measurable value of the quality characteristics of choice is used in this method. The Taguchi design flowchart is shown in Fig. 10. The signal-to-noise (S/N) ratio for the lower-the-

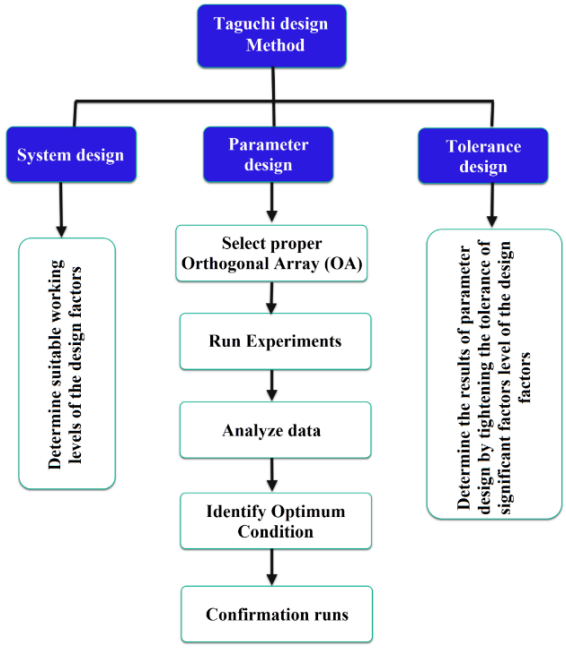

Fig. 10 Flowchart of Taguchi Design of Experiment

better case defined with the Taguchi method (Roy 2001) is given in Eq. (50)

$$S/N\ Ratio = -10\ \log\left[\sum \frac{y_i^2}{x}\right] \tag{50}$$

where, y_i is the value of optimization objective function, and n is the number of repetitions of optimization method in a trial for solving the problem. The levels of the Taguchi Design of Experiment method for the GOA (Saremi *et al.* 2017), DA (Mirjalili 2016), WOA (Mirjalili and Lewis 2016) and HHO (Heidari *et al.* 2019) algorithm are presented in Table 6. The results of Taguchi Design of Experiment are demonstrated in Fig. 11.

Table 6 Parameters for Taguchi DOE method

Optimization algorithm	Parameter	Level				
		1	2	3	4	5
GOA	Search Agent	20	25	30	35	40
	Iteration	300	350	400	450	500
	Attraction lenght scale	0.8	1	1.2	1.4	1.6
	Intensity of Attraction	0.3	0.4	0.5	0.6	0.7
DA	Search Agent	20	25	30	35	40
	Iteration	300	350	400	450	500
	Beta	0.8	1	1.2	1.4	1.6
WOA	Search Agent	20	25	30	35	40
	Iteration	300	350	400	450	500
	b	0.8	1	1.2	1.4	1.6
HHO	Search Agent	20	25	30	35	40
	Iteration	300	350	400	450	500
	Beta	0.8	1	1.2	1.4	1.6

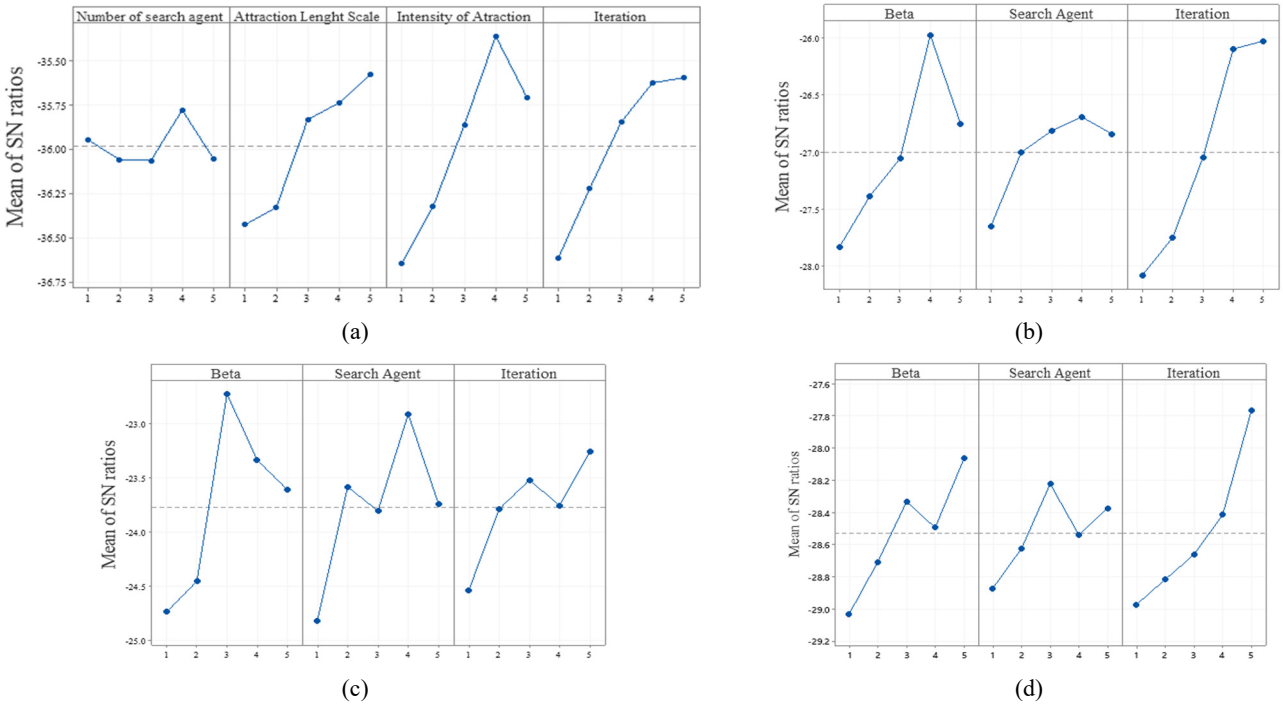

Fig. 11 Taguchi design parameters for (a) GOA; (b) DA; (c) WOA; and (d) HHO algorithms

7. Comparison of optimization algorithms

The accuracy of five optimization algorithms for the determination of the location and depth of a crack on the electrostatically actuated gas sensor with proof mass is investigated in this section. The parameters of the aforementioned optimization algorithms are tuned using Taguci design of experiment as detailed in Section 5. These parameters are summarized in Table 7. The results of the optimization algorithms are compared with the first four bending natural frequencies from theoretical calculations for the 12 cases presented in Table 3. The optimization results, relative error and objective cost functions for aforementioned optimization algorithms are presented in Table 8, Tables 9 and 10, respectively. The relative error estimation for the open edge crack in the sytem can be obtained using the following equation

$$\%Error = \left|\frac{Evaluated\ Value - Measured\ Value}{Measured\ Value}\right| \times 100 \quad (51)$$

The results from Table 8, Table 9 and Table 10 clearly show that the accuracy of the HHO is higher compared to GOA (Saremi *et al*. 2017), DA (Mirjalili 2016), WOA (Mirjalili and Lewis 2016) algorithms. More specifically, the average relative error of HHO in finding the location and depth of crack based of equation shown in Eq. (51) are 0.158% and 0.529%, respectively. The superiority of HHO compared to GOA, WOA and DA can be attributed to the features of the HHO algorithm that enhances the exploitation and exploration phases of HHO algorithm. More specifically, there are several diversification techniques based on the location of the hawks. Furthermore, the energy parameter of the HHO algorithm is used in order to improve the exploitation and exploration phases. Even though the accuracy of the HHO algorithm is quite high, there is still room for improvement the accuracy of algorithm for the crack detection application. There are studies, which address the balance between the exploration and exploitation phases for specific applications, in the literature. As one of the disadvantage, the HHO algorithm may be trapped in the local optima and consider the local optima as a global optima. Therefore, a hybrid algorithm

Table 7 Optimization parameters used in the crack detection

Optimization Algorithm	Parameter	Value
GOA	Search Agent	35
	Iteration	500
	Attraction lenght scale	0.6
	Intensity of Attraction	1.6
DA	Search Agent	35
	Iteration	500
	Beta	1.4
WOA	Search Agent	35
	Iteration	500
	b	1.2
HHO	Search Agent	30
	Iteration	500
	Beta	1.6
HHO-NM	Search Agent	30
	Iteration	500
	Beta	1.6

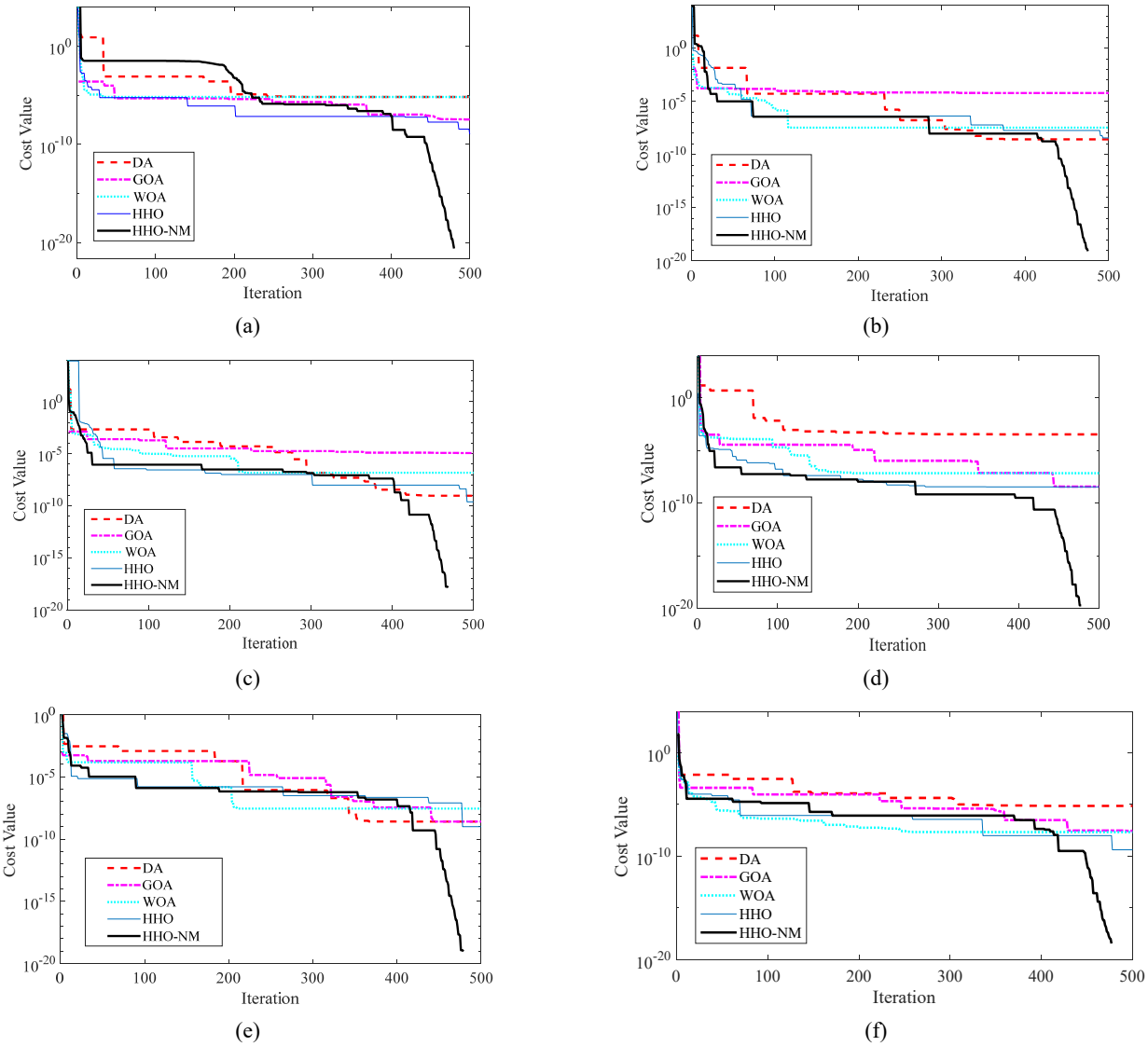

Fig. 12 The best cost value for (a) Test 1; (b) Test 3; (c) Test 5; (d) Test 7; (e) Test 9; and (f) Test 11

Table 8 The comparison of the results of optimization algorithms on the location and depth of the crack

TN	Actual value		Measured value									
			DA		GOA		WOA		HHO		HHO-NM	
	L	D	Location	Depth	Location	Depth	Location	Depth	Location	Depth	Location	Depth
1	0.2	0.1	0.197998	0.098652	0.201252	0.09947	1.99E-01	0.100706	0.200216	0.099977	**0.200024**	**0.099977**
2	0.2	0.15	0.200799	0.148846	0.199798	0.149324	2.02E-01	0.148748	0.200266	0.149946	**0.200182**	**0.149999**
3	0.2	0.2	0.200201	0.203681	0.201326	0.204557	2.00E-01	0.198489	0.199793	0.200836	**0.199979**	**0.200075**
4	0.4	0.1	0.400428	0.099857	0.400448	0.098026	4.02E-01	0.098718	0.400324	0.099947	**0.400203**	**0.099961**
5	0.4	0.15	0.400369	0.149877	0.400222	0.148375	4.00E-01	0.150641	0.402421	0.149917	**0.400002**	**0.149989**
6	0.4	0.2	0.402812	0.212267	0.401821	0.206829	4.02E-01	0.211403	0.40024	0.200836	**0.400202**	**0.200084**
7	0.6	0.1	0.598058	0.098665	0.600254	0.10136	6.00E-01	0.100309	0.599677	0.096210	**0.599968**	**0.09999**
8	0.6	0.15	0.601242	0.150424	0.600663	0.149857	6.02E-01	0.150537	0.600204	0.149902	**0.600204**	**0.14992**
9	0.6	0.2	0.600021	0.203068	0.600312	0.213522	6.00E-01	0.200705	0.602421	0.200832	**0.600421**	**0.20014**
10	0.8	0.1	0.801123	0.101413	0.804625	0.100456	8.00E-01	0.100613	0.800263	0.100013	**0.800206**	**0.100013**
11	0.8	0.15	0.802413	0.148879	0.802985	0.150337	8.00E-01	0.149865	0.802026	0.148666	**0.800003**	**0.15**
12	0.8	0.2	0.799808	0.198297	0.798257	0.200271	8.00E-01	0.198766	0.799748	0.199631	**0.799997**	**0.199963**

Table 9 Relative error between the actual and calculated crack dimension from optimization algorithms

Indicator	DA		GOA		WOA		HHO		HHO-NM	
	Location%	Depth%	Location%	Depth%	Location%	Depth%	Location%	Depth%	Location%	Depth%
Minimum	3.45E-03	0.08178	3.33E-02	0.09502	5.21E-03	0.012611	3.15E-02	0.013471	**3.15E-04**	**5.53E-05**
Average	2.02 E-01	1.38717	2.60 E-01	1.563603	2. 53E-01	1.0037	1. 58E-01	0.529	**2.85E-02**	**0.025568**
Maximum	1.03E+00	6.300021	6.63E-01	6.761138	1.10E+00	5.701475	6.05E-01	3.800002	**9.10E-02**	**0.07**

Table 10 Optimization cost value for the optimization algorithm

TN	Evaluated cost value				
	DA	GOA	WOA	HHO	HHO-NM
1	6.79E-06	3.51E-08	6.79E-06	1.25E-09	2.24E-20
2	1.49E-09	5.10E-08	1.03E-05	1.49E-09	1.58E-18
3	2.67E-09	6.04E-05	3.36E-08	2.67E-09	8.34E-20
4	1.10E-08	4.29E-06	4.78E-06	1.84E-10	1.26E-19
5	9.28E-10	1.16E-05	1.48E-07	9.28E-10	1.43E-18
6	1.59E-05	3.14E-10	8.17E-06	3.14E-10	2.84E-20
7	0.000349	3.68E-09	6.96E-08	3.52E-09	3.71E-19
8	2.32E-09	8.51E-09	6.14E-07	2.32E-09	2.63E-19
9	2.54E-09	2.54E-09	2.81E-08	2.54E-09	1.61E-20
10	2.01E-06	3.29E-07	3.83E-09	3.62E-10	3.77E-19
11	7.16E-06	2.84E-08	2.13E-08	2.27E-08	5.98E-18
12	2.06E-08	1.24E-08	2.18E-08	2.06E-09	1.71E-20

based on Nelder Mead is proposed to enhance the performance of HHO algorithm and avoid local optima stagnation in this study.

The best cost value versus number of iterations is plotted in Fig. 12 for all 12 cases. The results demonstate the superiority of HHO-NM algorithm compared to the other algorithms for the crack detection application. It can be observed from Fig. 12 that the speed of convergence is improved with the proposed hybrid algorithm (HHO-NM). The results from Table 8 indicate that HHO-NM can predict the crack parameters more accurately. More specifically, the average error for the location of the crack is 0.0285% and its average error in finding the depth is 0.025568% as can been from Table 9.

8. Conclusions

In this study, the effect of crack on the mechanical behavior of electrostatically actuated microcantilever with a tip mass as a representation of gas sensor is investigated. Besides, a novel hybrid algorithm is proposed to determine the location and depth of the crack on the microsystem. The static deflection and natural frequency of the system are obtained using exact method where the equations of motion are solved using the perturbation method. In the first part of paper, the effect of crack on the both static and dynamic pull-in is analyzed. It is shown that a crack can affect the pull-in instability. The results show that the length of the crack is more dominant than the depth of the crack.

We proposed a novel hybrid metaheuristic algorithm to detect the location and position of the crack in the second part of the paper. The proposed HHO-NM hybrid algorithm is more accurate and efficient compared to the well-known conventional algorithms (WOA-DA-GOA-HHO) from the literature. The parameters of optimization algorithms are tuned using Taguchi design of experiment (DOE) method for a fair comparison of the results. The results showed the superiority of the proposed algorithm in term of accuracy in finding cracks parameters. The proposed algorithm is expected to prove beneficial where the accuracy and efficiency of the determination of the crack parameters are important for critical engineering applications.

References

Abbasi, A., Firouzi, B. and Sendur, P. (2019), "On the application of Harris hawks optimization (HHO) algorithm to the design of microchannel heat sinks", *Eng. Comput.*, **37**, 1409-1428. https://doi.org/10.1007/s00366-019-00892-0

Abdalla, M.M., Reddy, C.K., Faris, W.F. and Gurdal, Z. (2005), "Optimal design of an electrostatically actuated microbeam for maximum pull-in voltage", *Comput. Struct.*, **83**(15-16), 1320-1329. https://doi.org/10.1016/j.compstruc.2004.07.010

Akbas, S.D. (2018), "Forced vibration analysis of cracked functionally graded microbeams", *Adv. Nano Res., Int. J.*, **6**(1), 39-55. http://dx.doi.org/10.12989/anr.2018.6.1.039

Aleem, S.H.A., Zobaa, A.F., Balci, M.E. and Ismael, S.M. (2019), "Harmonic overloading minimization of frequency-dependent components in harmonics polluted distribution systems using Harris hawks optimization algorithm", *IEEE Access*, **7**, 100824-100837. https://doi.org/10.1109/ACCESS.2019.2930831

Al-Basyouni, K.S., Tounsi, A. and Mahmoud, S.R. (2015), "Size dependent bending and vibration analysis of functionally graded micro beams based on modified couple stress theory and neutral surface position", *Compos. Struct.*, **125**, 621-630. https://doi.org/10.1016/j.compstruct.2014.12.070

Amouzgar, K., Bandaru, S. andersson, T. and Ng, A.H. (2020), "Metamodel-based multi-objective optimization of a turning process by using finite element simulation", *Eng. Optimiz.*, **52**(7), 1261-1278. https://doi.org/10.1080/0305215X.2019.1639050

Bansal, D., Bajpai, A., Kumar, P., Kaur, M. and Kumar, A. (2020), "Effect of Stress on Pull-in Voltage of RF MEMS SPDT Switch", *IEEE Transact. Electron Devices*, **67**(5), 2147-2152. https://doi.org/10.1109/TED.2020.2982667

Bianchi, G. and Radi, E. (2020), "Analytical estimates of the pull-in voltage or carbon nanotubes considering tip-charge concentration and intermolecular forces", *Meccanica*, **55**(1), 193-209. https://doi.org/10.1007/s11012-019-01119-8

Cao, B., Zhao, J., Yang, P., Gu, Y., Muhammad, K., Rodrigues, J.J. and de Albuquerque, V.H.C. (2019a), "Multiobjective 3-D

topology optimization of next-generation wireless data center network", *IEEE Transact. Indust. Inform.*, **16**(5), 3597-3605. https://doi.org/10.1109/TII.2019.2952565

Cao, B., Zhao, J., Gu, Y., Fan, S. and Yang, P. (2019b), "Security-aware industrial wireless sensor network deployment optimization", *IEEE Transact. Industr. Inform*, **16**(8), 5309-5316. https://doi.org/10.1109/TII.2019.2961340

Cao, B., Dong, W., Lv, Z., Gu, Y., Singh, S. and Kumar, P. (2020a), "Hybrid microgrid many-objective sizing optimization with fuzzy decision", *IEEE Transact. Fuzzy Syst.*, **28**(11), 2702-2710. https://doi.org/10.1109/TFUZZ.2020.3026140

Cao, B., Fan, S., Zhao, J., Yang, P., Muhammad, K. and Tanveer, M. (2020b), "Quantum-enhanced multiobjective large-scale optimization via parallelism", *Swarm Evolut. Comput.*, **57**, 100697. https://doi.org/10.1016/j.swevo.2020.100697

Cao, Y., Li, Y., Zhang, G., Jermsittiparsert, K. and Nasseri, M. (2020c), "An efficient terminal voltage control for PEMFC based on an improved version of whale optimization algorithm", *Energy Reports*, **6**, 530-542. https://doi.org/10.1016/j.egyr.2020.02.035

Cao, B., Wang, X., Zhang, W., Song, H. and Lv, Z. (2020d), "A many-objective optimization model of industrial internet of things based on private blockchain", *IEEE Network*, **34**(5), 78-83. https://doi.org/10.1109/MNET.011.1900536

Cao, B., Zhao, J., Gu, Y., Ling, Y. and Ma, X. (2020e), "Applying graph-based differential grouping for multiobjective large-scale optimization", *Swarm Evolut. Comput.*, **53**, 100626. https://doi.org/10.1016/j.swevo.2019.100626

Casciati, S. (2008), "Stiffness identification and damage localization via differential evolution algorithms", *Structural Control and Health Monitoring: The Official Journal of the International Association for Structural Control and Monitoring and of the European Association for the Control of Structures*, **15**(3), 436-449. https://doi.org/10.1002/stc.236

Chen, Y., He, L., Guan, Y., Lu, H. and Li, J. (2017), "Life cycle assessment of greenhouse gas emissions and water-energy optimization for shale gas supply chain planning based on multi-level approach: Case study in Barnett, Marcellus, Fayetteville, and Haynesville shales", *Energy Convers. Manage.*, **134**, 382-398. ttps://doi.org/10.1016/j.enconman.2016.12.019

Chen, Y., He, L., Li, J. and Zhang, S. (2018), "Multi-criteria design of shale-gas-water supply chains and production systems towards optimal life cycle economics and greenhouse gas emissions under uncertainty", *Comput. Chem. Eng.*, **109**, 216-235. https://doi.org/10.1016/j.compchemeng.2017.11.014

Chen, H., Heidari, A.A., Chen, H., Wang, M., Pan, Z. and Gandomi, A.H. (2020), "Multi-population differential evolution-assisted Harris hawks optimization: Framework and case studies", *Future Gener. Comput. Syst.*, **111**, 175-198. https://doi.org/10.1016/j.future.2020.04.008

Cheng, X., He, L., Lu, H., Chen, Y. and Ren, L. (2016), "Optimal water resources management and system benefit for the Marcellus shale-gas reservoir in Pennsylvania and West Virginia", *J. Hydrol.*, **540**, 412-422. https://doi.org/10.1016/j.jhydrol.2016.06.041

Dastjerdi, S. and Abbasi, M. (2019), "A vibration analysis of a cracked micro-cantilever in an atomic force microscope by using transfer matrix method", *Ultramicroscopy*, **196**, 33-39. https://doi.org/10.1016/j.ultramic.2018.09.014

Deng, Y., Zhang, T., Sharma, B.K. and Nie, H. (2019), "Optimization and mechanism studies on cell disruption and phosphorus recovery from microalgae with magnesium modified hydrochar in assisted hydrothermal system", *Sci. Total Environ.*, **646**, 1140-1154. https://doi.org/10.1016/j.scitotenv.2018.07.369

Duan, J.S. and Rach, R. (2013), "A pull-in parameter analysis for the cantilever NEMS actuator model including surface energy, fringing field and Casimir effects", *Int. J. Solids Struct.*, **50**(22-23), 3511-3518. https://doi.org/10.1016/j.ijsolstr.2013.06.012

Ekinci, S., Hekimoğlu, B., Demirören, A. and Kaya, S. (2019), "Harris Hawks Optimization Approach for Tuning of FOPID Controller in DC-DC Buck Converter", *Proceedings of 2019 International Artificial Intelligence and Data Processing Symposium* (*IDAP*), pp. 1-9.

Firouzi, B. and Zamanian, M. (2019), "The effect of capillary and intermolecular forces on instability of the electrostatically actuated microbeam with T-shaped paddle in the presence of fringing field", *Appl. Mathe. Modell.*, **71**, 243-268. https://doi.org/10.1016/j.apm.2019.02.016

Firouzi, B., Zamanian, M. and Hosseini, S.A.A. (2016), "Static and dynamic responses of a microcantilever with a T-shaped tip mass to an electrostatic actuation", *Acta Mechanica Sinica*, **32**(6), 1104-1122. https://doi.org/10.1007/s10409-016-0596-9

Hagedorn, P. and DasGupta, A. (2007), *Vibrations and Waves in Continuous Mechanical Systems*, pp. 113-120, Chichester, Wiley.

Hassannejad, R. and Amiri Jahed, S. (2018), "Nonlinear Dynamic Analysis of Cracked Micro-Beams Below and at the Onset of Dynamic Pull-In Instability", *J. Solid Mech.*, **10**(1), 110-123.

He, R.S. and Hwang, S.F. (2006), "Damage detection by an adaptive real-parameter simulated annealing genetic algorithm", *Comput. Struct.*, **84**(31-32), 2231-2243. https://doi.org/10.1016/j.compstruc.2006.08.031

He, Y., Guo, D. and Chu, F. (2001), "Using genetic algorithms and finite element methods to detect shaft crack for rotor-bearing system", *Mathe. Comput. Simul.*, **57**(1-2), 95-108. https://doi.org/10.1016/S0378-4754(01)00295-6

He, L., Chen, Y. and Li, J. (2018a), "A three-level framework for balancing the tradeoffs among the energy, water, and air-emission implications within the life-cycle shale gas supply chains", *Resour. Conserv. Recycl.*, **133**, 206-228. https://doi.org/10.1016/j.resconrec.2018.02.015

He, L., Chen, Y., Zhao, H., Tian, P., Xue, Y. and Chen, L. (2018b), "Game-based analysis of energy-water nexus for identifying environmental impacts during Shale gas operations under stochastic input", *Sci. Total Environ.*, **627**, 1585-1601. https://doi.org/10.1016/j.scitotenv.2018.02.004

Heidari, A.A., Mirjalili, S., Faris, H., Aljarah, I., Mafarja, M. and Chen, H. (2019), "Harris hawks optimization: Algorithm and applications", *Future Generat. Comput. Syst.*, **97**, 849-872. https://doi.org/10.1016/j.future.2019.02.028

Huang, X., Yang, M., Feng, L., Gu, H., Su, H., Cui, X. and Cao, W. (2017), "Crack detection study for hydraulic concrete using PPP-BOTDA", *Smart Struct. Syst., Int. J.*, **20**(1), 75-83. https://doi.org/10.12989/sss.2017.20.1.075

Jena, P.K. and Parhi, D.R. (2015), "A modified particle swarm optimization technique for crack detection in Cantilever Beams", *Arab. J. Sci. Eng.*, **40**(11), 3263-3272. https://doi.org/10.1007/s13369-015-1661-6

Jena, P.K., Thatoi, D.N. and Parhi, D.R. (2015), "Dynamically self-adaptive fuzzy PSO technique for smart diagnosis of transverse crack", *Appl. Artif. Intell.*, **29**(3), 211-232. https://doi.org/10.1080/08839514.2015.1004611

Khater, M.E., Al-Ghamdi, M., Park, S., Stewart, K.M., Abdel-Rahman, E.M., Penlidis, A. and Basha, M. (2014), "Binary MEMS gas sensors", *J. Micromech. Microeng.*, **24**(6), 065007. https://doi.org/10.1088/0960-1317/24/6/065007

Khatir, S., Dekemele, K., Loccufier, M., Khatir, T. and Wahab, M. A. (2018), "Crack identification method in beam-like structures using changes in experimentally measured frequencies and Particle Swarm Optimization", *Comptes Rendus*

Mécanique, **346**(2), 110-120. https://doi.org/10.1016/j.crme.2017.11.008

Liu, E., Lv, L., Yi, Y. and Xie, P. (2019), "Research on the steady operation optimization model of natural gas pipeline considering the combined operation of air coolers and compressors", *IEEE Access*, **7**, 83251-83265.

Ma, X., Foong, L.K., Morasaei, A., Ghabussi, A. and Lyu, Z. (2020), "Swarm-based hybridizations of neural network for predicting the concrete strength", *Smart Struct. Syst., Int. J.*, **26**(2), 241-251. https://doi.org/10.12989/sss.2020.26.2.241

Mirjalili, S. (2016) "Dragonfy algorithm: a new meta-heuristic optimization technique for solving single-objective, discrete, and multi-objective problems", *Neural Comput. Appl.*, **27**(4), 1053-1073. https://doi.org/10.1007/s00521-015-1920-1

Mirjalili, S. and Lewis, A. (2016), "The whale optimization algorithm", *Adv. Eng. Software*, **95**, 51-67. https://doi.org/10.1016/j.advengsoft.2016.01.008

Moezi, S.A., Zakeri, E., Zare, A. and Nedaei, M. (2015), "On the application of modified cuckoo optimization algorithm to the crack detection problem of cantilever Euler–Bernoulli beam", *Comput. Struct.*, **157**, 42-50. https://doi.org/10.1016/j.compstruc.2015.05.008

Moezi, S.A., Zakeri, E. and Zare, A. (2018a), "A generally modified cuckoo optimization algorithm for crack detection in cantilever Euler-Bernoulli beams", *Precision Eng.*, **52**, 227-241. https://doi.org/10.1016/j.precisioneng.2017.12.010

Moezi, S.A., Zakeri, E. and Zare, A. (2018b), "Structural single and multiple crack detection in cantilever beams using a hybrid Cuckoo-Nelder-Mead optimization method", *Mech. Syst. Signal Process.*, **99**, 805-831. https://doi.org/10.1016/j.ymssp.2017.07.013

Moradi, S., Razi, P. and Fatahi, L. (2011), "On the application of bees algorithm to the problem of crack detection of beam-type structures", *Comput. Struct.*, **89**(23-24), 2169-2175. https://doi.org/10.1016/j.compstruc.2011.08.020

Motallebi, A., Fathalilou, M. and Rezazadeh, G. (2012), "Effect of the open crack on the pull-in instability of an electrostatically actuated micro-beam", *Acta Mechanica Solida Sinica*, **25**(6), 627-637. https://doi.org/10.1016/S0894-9166(12)60058-5

Nayfeh, A.H., Ouakad, H.M., Najar, F., Choura, S. and Abdel-Rahman, E.M. (2010), "Nonlinear dynamics of a resonant gas sensor", *Nonlinear Dyn.*, **59**(4), 607-618. https://doi.org/10.1007/s11071-009-9567-z

Nelder, J.A. and Mead, R. (1965), "A simplex method for function minimization", *Comput. J.*, **7**(4), 308-313. https://doi.org/10.1093/comjnl/7.4.308

Ouakad, H.M. (2015), "The response of a micro-electro-mechanical system (MEMS) cantilever-paddle gas sensor to mechanical shock loads", *J. Vib. Control*, **21**(14), 2739-2754. https://doi.org/10.1177/1077546313514763

Ouakad, H.M. and Younis, M.I. (2008), "Modelling and simulation of a cantilever-paddle beam under the effect of capillary, shock, and electrostatic forces", *Proceedings of ASME 2008 International Design Engineering Technical Conferences and Computers and Information in Engineering Conference* (pp. 677-682), American Society of Mechanical Engineers Digital Collection.

Pawar, P.M. and Ganguli, R. (2003), "Genetic fuzzy system for damage detection in beams and helicopter rotor blades", *Comput. Methods Appl. Mech. Eng.*, **192**(16-18), 2031-2057. https://doi.org/10.1016/S0045-7825(03)00237-8

Qu, S., Han, Y., Wu, Z. and Raza, H. (2020), "Consensus modeling with asymmetric cost based on data-driven robust optimization", *Group Decision and Negotiation*, 1-38. https://doi.org/10.1007/s10726-020-09707-w

Rajabi, M., Shamshirsaz, M. and Naraghi, M. (2017), "Crack detection in rectangular plate by electromechanical impedance method: modeling and experiment", *Smart Struct. Syst., Int. J.*, **19**(4), 361-369. https://doi.org/10.12989/sss.2017.19.4.361

Rajan, A. and Malakar, T. (2015), "Optimal reactive power dispatch using hybrid Nelder–Mead simplex based firefly algorithm", *Int. J. Electr. Power Energy Syst.*, **66**, 9-24. https://doi.org/10.1016/j.ijepes.2014.10.041

Rezaiee-Pajand, M. and Tavakoli, F.H. (2015), "Crack detection in concrete gravity dams using a genetic algorithm", *Proceedings of the Institution of Civil Engineers-Structures and Buildings*, **168**(3), 192-209.

Roy, R.K. (2001), *Design of experiments using the Taguchi approach: 16 steps to product and process improvement*, John Wiley and Sons.

Roy, D.K., Barzegar, R., Quilty, J. and Adamowski, J. (2020), "Using ensembles of adaptive neuro-fuzzy inference system and optimization algorithms to predict reference evapotranspiration in subtropical climatic zones", *J. Hydrol.*, **591**, 125509. https://doi.org/10.1016/j.jhydrol.2020.125509

Sahoo, B. and Maity, D. (2007), "Damage assessment of structures using hybrid neuro-genetic algorithm", *Appl. Soft Comput.*, **7**(1), 89-104. https://doi.org/10.1016/j.asoc.2005.04.001

Sarakhsi, M.K., Ghomi, S.F. and Karimi, B. (2016), "A new hybrid algorithm of scatter search and Nelder–Mead algorithms to optimize joint economic lot sizing problem", *J. Computat. Appl. Mathe.*, **292**, 387-401. https://doi.org/10.1016/j.cam.2015.07.027

Saremi, S., Mirjalili, S. and Lewis, A. (2017), "Grasshopper optimisation algorithm: theory and application", *Adv. Eng Softw.*, **105**, 30-47. https://doi.org/10.1016/j.advengsoft.2017.01.004

Shaat, M., Khorshidi, M.A., Abdelkefi, A. and Shariati, M. (2016), "Modeling and vibration characteristics of cracked nano-beams made of nanocrystalline materials", *Int. J. Mech. Sci.*, **115**, 574-585. https://doi.org/10.1016/j.ijmecsci.2016.07.037

Shen, L., Chen, H., Yu, Z., Kang, W., Zhang, B., Li, H. and Liu, D. (2016), "Evolving support vector machines using fruit fly optimization for medical data classification", *Knowl.-Based Syst.*, **96**, 61-75. https://doi.org/10.1016/j.knosys.2016.01.002

Sourki, R. and Hoseini, S.A.H. (2016), "Free vibration analysis of size-dependent cracked microbeam based on the modified couple stress theory", *Appl. Phys. A*, **122**(4), 413. https://doi.org/10.1007/s00339-016-9961-6

Sun, G., Yang, B., Yang, Z. and Xu, G. (2019), "An adaptive differential evolution with combined strategy for global numerical optimization", *Soft Computing*, **24**, 6277-6296. https://doi.org/10.1007/s00500-019-03934-3

Sutar, M.K., Pattnaik, S. and Modi, P.K. (2021), "Parametric Optimization of Cracked Cantilever Beam Using Genetic Algorithm", *Trends Manuf. Eng. Manage.*, 915-921. https://doi.org/10.1007/978-981-15-4745-4_79

Too, J., Abdullah, A.R. and Mohd Saad, N. (2019), "A new quadratic binary harris hawk optimization for feature selection", *Electronics*, **8**(10), 1130. https://doi.org/10.3390/electronics8101130

Vakil-Baghmisheh, M.T., Peimani, M., Sadeghi, M.H. and Ettefagh, M.M. (2008), "Crack detection in beam-like structures using genetic algorithms", *Appl. Soft Comput.*, **8**(2), 1150-1160. https://doi.org/10.1016/j.asoc.2007.10.003

Vakil-Baghmisheh, M.V., Peimani, M., Sadeghi, M.H., Ettefagh, M.M. and Tabrizi, A.F. (2012), "A hybrid particle swarm–Nelder–Mead optimization method for crack detection in cantilever beams", *Appl. Soft Comput.*, **12**(8), 2217-2226. https://doi.org/10.1016/j.asoc.2012.03.030

Wang, M., Chen, H., Yang, B., Zhao, X., Hu, L., Cai, Z, and Tong, C. (2017), "Toward an optimal kernel extreme learning machine using a chaotic moth-flame optimization strategy with applications in medical diagnoses", *Neurocomputing*, **267**, 69-

84. https://doi.org/10.1016/j.neucom.2017.04.060
Xiang, J., Zhong, Y., Chen, X. and He, Z. (2008), "Crack detection in a shaft by combination of wavelet-based elements and genetic algorithm", *Int. J. Solids Struct.*, **45**(17), 4782-4795. https://doi.org/10.1016/j.ijsolstr.2008.04.014
Yang, X.S. (2010), *Nature-inspired Metaheuristic Algorithms*, Luniver Press.
Ye, X., Lyu, Z. and Foong, L.K. (2020a), "Hybridized dragonfly, whale and ant lion algorithms in enlarged pile's behavior", *Smart Struct. Syst., Int. J.*, **25**(6), 765-778. https://doi.org/10.12989/sss.2020.25.6.765
Ye, X., Moayedi, H., Khari, M. and Foong, L.K. (2020b). "Metaheuristic-hybridized multilayer perceptron in slope stability analysis", *Smart Struct. Syst., Int. J.*, **26**(3), 263-275. https://doi.org/10.12989/sss.2020.26.3.263
Yildiz, A.R., Yildiz, B.S., Sait, S.M. and Li, X. (2019a), "The Harris hawks, grasshopper and multi-verse optimization algorithms for the selection of optimal machining parameters in manufacturing operations", *Mater. Test*, **61**(8), 725-733. https://doi.org/10.3139/120.111377
Yildiz, A.R., Yildiz, B.S., Sait, S.M., Bureerat, S. and Pholdee, N. (2019b), "A new hybrid Harris hawks–Nelder–Mead optimization algorithm for solving design and manufacturing problems", *Mater. Test*, **61**(8), 735-743. https://doi.org/10.3139/120.111378
Younis, M.I. (2011), *MEMS Linear and Nonlinear Statics and Dynamics*, (Vol. 20), Springer Science and Business Media.
Zamanian, M., Javadi, S., Firouzi, B. and Hosseini, S.A.A. (2018), "Modeling and analysis of power harvesting by a piezoelectric layer coated on an electrostatically actuated microcantilever", *Mater. Res. Express*, **5**(12), 125502. https://doi.org/10.1088/2053-1591/aadf15
Zhang, J. and Fu, Y. (2012), "Pull-in analysis of electrically actuated viscoelastic microbeams based on a modified couple stress theory", *Meccanica*, **47**(7), 1649-1658. https://doi.org/10.1007/s11012-012-9545-2
Zhang, X., Gao, R.X., Yan, R., Chen, X., Sun, C. and Yang, Z. (2016), "Multivariable wavelet finite element-based vibration model for quantitative crack identification by using particle swarm optimization", *J. Sound Vib.*, **375**, 200-216. https://doi.org/10.1016/j.jsv.2016.04.018
Zhou, H., Zhang, W.M., Peng, Z.K. and Meng, G. (2015), "Dynamic characteristics of electrostatically actuated microbeams with slant crack", *Mathe. Problems Eng.* https://doi.org/10.1155/2015/208065

HJ

APPENDIX 1

$$\frac{\partial^4 u_1}{\partial \hat{x}^4}+\frac{\partial^2 u_1}{\partial \hat{t}^2}+\alpha_5\frac{\partial u_1}{\partial t}=0 \quad ,0\le \hat{x}\le \hat{l}_c$$

$$\frac{\partial^4 u_2}{\partial \hat{x}^4}+\frac{\partial^2 u_2}{\partial \hat{t}^2}+\alpha_5\frac{\partial u_2}{\partial t}=-\alpha_3\left[\frac{\partial^2 u_2}{\partial \hat{t}^2}|\hat{x}=l\right]\delta(\hat{x}-\hat{l})+$$
$$2\alpha_{el}{V_{DC}}^2\left[\int_L^{L+2l_p}\frac{u_3(x,t)}{(1-w_{s3}(\hat{x}))^3}d\hat{x}\right]\delta(\hat{x}-\hat{l})+$$
$$\alpha_{fr}{V_{DC}}^2\left[\int_L^{L+2l_p}\frac{u_3(x,t)}{(1-w_{s3}(\hat{x}))^2}d\hat{x}\right]\delta(\hat{x}-\hat{l})$$
$$3\alpha_{el}{V_{DC}}^2\left[\int_L^{L+2l_p}\frac{{u_3}^2(x,t)}{(1-w_{s2}(\hat{x}))^4}d\hat{x}\right]\delta(\hat{x}-\hat{l})+$$
$$4\alpha_{el}{V_{DC}}^2\left[\int_L^{L+2l_p}\frac{{u_3}^3(x,t)}{(1-w_{s3}(\hat{x}))^5}d\hat{x}\right]\delta(\hat{x}-\hat{l})$$
$$+\alpha_{fr}{V_{DC}}^2\left[\int_L^{L+2l_p}\frac{u_3(x,t)}{(1-w_{s2}(\hat{x}))^3}d\hat{x}\right]\delta(\hat{x}-\hat{l})+$$
$$\alpha_{fr}{V_{DC}}^2\left[\int_L^{L+2l_p}\frac{{u_3}^3(x,t)}{(1-w_{s3}(\hat{x}))^4}d\hat{x}\right]\delta(\hat{x}-\hat{l})$$
$$-\alpha_4\left[\frac{\partial^3 u_1}{\partial \hat{x}\partial \hat{t}^2}|\hat{x}=l\right]\frac{\partial\delta(\hat{x}-\hat{l})}{\partial\hat{x}}-\left[\int_L^{L+2l_p}\hat{c}\dot{u}_3\ dx\right]\delta(\hat{x}-\hat{l})+$$
$$2\alpha_{el}{V_{DC}}^2\left[\int_L^{L+2l_p}\frac{(\hat{x}-(\hat{l}+\hat{l}_p))u_3(x,t)}{(1-w_{s3}(\hat{x}))^3}d\hat{x}\right]\frac{\partial\delta(\hat{x}-\hat{l})}{\partial\hat{x}}+$$
$$\alpha_{fr}{V_{DC}}^2\left[\int_L^{L+2l_p}\frac{(\hat{x}-(\hat{l}+\hat{l}_p))u_3(x,t)}{(1-w_{s3}(\hat{x}))^2}d\hat{x}\right]\frac{\partial\delta(\hat{x}-\hat{l})}{\partial\hat{x}}+$$
$$3\alpha_{el}{V_{DC}}^2\left[\int_L^{L+2l_p}\frac{(\hat{x}-(\hat{l}+\hat{l}_p)){u_3}^2(x,t)}{(1-w_{s3}(\hat{x}))^4}d\hat{x}\right]\frac{\partial\delta(\hat{x}-\hat{l})}{\partial\hat{x}}+$$
$$4\alpha_{el}{V_{DC}}^2\left[\int_L^{L+2l_p}\frac{(\hat{x}-(\hat{l}+\hat{l}_p)){u_3}^3(x,t)}{(1-w_{s3}(\hat{x}))^5}d\hat{x}\right]\frac{\partial\delta(\hat{x}-\hat{l})}{\partial\hat{x}}$$
$$+\alpha_{fr}{V_{DC}}^2\left[\int_L^{L+2l_p}\frac{(\hat{x}-(\hat{l}+\hat{l}_p)){u_3}^2(x,t)}{(1-w_{s3}(\hat{x}))^3}d\hat{x}\right]\frac{\partial\delta(\hat{x}-\hat{l})}{\partial\hat{x}}+$$
$$\alpha_{fr}{V_{DC}}^2\left[\int_L^{L+2l_p}\frac{(\hat{x}-(\hat{l}+\hat{l}_p)){u_3}^3(x,t)}{(1-w_{s3}(\hat{x}))^4}d\hat{x}\right]\frac{\partial\delta(\hat{x}-\hat{l})}{\partial\hat{x}}$$
$$+2\alpha_{el}V_{DC}V_{AC}\cos(\Omega t)\frac{\partial\delta(\hat{x}-\hat{l})}{\partial\hat{x}}\left[\int_L^{L+2l_p}\frac{1}{(1-w_{s3}(\hat{x}))^3}d\hat{x}\right]\delta(\hat{x}-\hat{l})-$$
$$\left[\int_L^{L+2l_p}\hat{c}\big(\hat{x}-(\hat{l}+\hat{l}_p)\big)\dot{u}_3\ d\hat{x}\right]\frac{\partial\delta(\hat{x}-\hat{l})}{\partial\hat{x}}$$
$$+2\alpha_{fr}V_{DC}V_{AC}\cos(\Omega t)\frac{\partial\delta(\hat{x}-\hat{l})}{\partial\hat{x}}\left[\int_L^{L+2l_p}\frac{1}{(1-w_{s3}(\hat{x}))^2}d\hat{x}\right]\delta(\hat{x}-\hat{l})+$$
$$2\alpha_{el}V_{DC}V_{AC}\cos(\Omega t)\left[\int_L^{L+2l_p}\frac{(\hat{x}-l_c)}{(1-w_{s3}(\hat{x}))^3}d\hat{x}\right]\frac{\partial\delta(\hat{x}-\hat{l})}{\partial\hat{x}}+$$
$$2\alpha_{fr}V_{DC}V_{AC}\cos(\Omega t)\left[\int_L^{L+2l_p}\frac{(\hat{x}-l_c)}{(1-w_{s3}(\hat{x}))^2}d\hat{x}\right]\frac{\partial\delta(\hat{x}-\hat{l})}{\partial\hat{x}} \quad ,\hat{l}_c\le\hat{x}\le\hat{l}$$

APPENDIX 2

$$M_1 = \int_{\hat{l}_c}^{\hat{l}} \left\{ \frac{\partial^4 \varphi_2}{\partial x^4} - 2\alpha_{el} {V_{DC}}^2 \left[\int_{\hat{l}}^{\hat{l}+2\hat{l}_p} \frac{\varphi_3}{(1-w_{s3}(\hat{x}))^3} d\hat{x} \right] Dirac(\hat{x}-\hat{l}) \right\} \varphi_2 d\hat{x}$$
$$+2\alpha_{el} {V_{DC}}^2 \int_{\hat{l}_c}^{\hat{l}} \left[\int_{\hat{l}}^{\hat{l}+2\hat{l}_p} \frac{\left(\hat{x}-\left(\hat{l}+\hat{l}_p\right)\right)\varphi_3}{\left(1-w_{s3}(\hat{x})\right)} d\hat{x} \right] \frac{\partial Dirac(\hat{x}-\hat{l})}{\partial \hat{x}} \varphi_2 d\hat{x}$$
$$-\alpha_{fr} {V_{DC}}^2 \left[\int_{\hat{l}_c}^{\hat{l}} \int_{\hat{l}}^{\hat{l}+2\hat{l}_p} \frac{\varphi_3(\hat{x},t)}{(1-w_{s3}(\hat{x}))^2} d\hat{x} \right] Dirac(\hat{x}-\hat{l}) \varphi_2 d\hat{x}$$
$$+\alpha_{fr} {V_{DC}}^2 \int_{\hat{l}_c}^{\hat{l}} \left[\int_{\hat{l}}^{\hat{l}+2\hat{l}_p} \frac{(\hat{x}-(\hat{l}+\hat{l}_p))\varphi_3}{(1-w_{s3}(\hat{x}))^2} d\hat{x} \right] \frac{\partial Dirac(\hat{x}-\hat{l})}{\partial \hat{x}} \varphi_2 d\hat{x} + \int_0^{\hat{l}_c} \frac{\partial^4 \varphi_1}{\partial x^4} \varphi_1 d\hat{x}$$

$$M_2 = -3\alpha_{el} {V_{DC}}^2 \int_{\hat{l}_c}^{\hat{l}} \left[\int_{\hat{l}}^{\hat{l}+2\hat{l}_p} \frac{{\varphi_3}^2}{(1-w_{s3}(\hat{x}))^4} d\hat{x} \right] Dirac(\hat{x}-\hat{l}) \varphi_2 d\hat{x}$$
$$+3\alpha_{el} {V_{DC}}^2 \int_{\hat{l}_c}^{\hat{l}} \left[\int_{\hat{l}}^{\hat{l}+2\hat{l}_p} \frac{\left(\hat{x}-\left(\hat{l}+\hat{l}_p\right)\right){\varphi_3}^2}{(1-w_{s3}(\hat{x}))^4} d\hat{x} \right] \frac{\partial Dirac(\hat{x}-\hat{l})}{\partial \hat{x}} \varphi_2 d\hat{x}$$
$$-\alpha_{fr} {V_{DC}}^2 \left[\int_{\hat{l}_c}^{\hat{l}} \int_{\hat{l}}^{\hat{l}+2\hat{l}_p} \frac{{\varphi^2}_3(\hat{x},t)}{(1-w_{s3}(\hat{x}))^3} d\hat{x} \right] Dirac(\hat{x}-\hat{l}) \varphi_2 d\hat{x}$$
$$+\alpha_{fr} {V_{DC}}^2 \int_{\hat{l}_c}^{\hat{l}} \left[\int_{\hat{l}}^{\hat{l}+2\hat{l}_p} \frac{\left(\hat{x}-\left(\hat{l}+\hat{l}_p\right)\right){\varphi_3}^2}{(1-w_{s3}(\hat{x}))^3} d\hat{x} \right] \frac{\partial Dirac(\hat{x}-\hat{l})}{\partial \hat{x}} \varphi_2 d\hat{x} +$$

$$M_3 = -4\alpha_{el} {V_{DC}}^2 \int_{\hat{l}_c}^{\hat{l}} \left[\int_{\hat{l}}^{\hat{l}+2\hat{l}_p} \frac{{\varphi_3}^3}{(1-w_{s3}(\hat{x}))^5} d\hat{x} \right] Dirac(\hat{x}-\hat{l}) \varphi_2 d\hat{x}$$
$$+4\alpha_{el} {V_{DC}}^2 \int_{\hat{l}_c}^{\hat{l}} \left[\int_{\hat{l}}^{\hat{l}+2\hat{l}_p} \frac{\left(\hat{x}-\left(\hat{l}+\hat{l}_p\right)\right){\varphi_3}^3}{(1-w_{s3}(\hat{x}))^5} d\hat{x} \right] \frac{\partial Dirac(\hat{x}-\hat{l})}{\partial \hat{x}} \varphi_2 d\hat{x}$$
$$-\alpha_{fr} {V_{DC}}^2 \left[\int_{\hat{l}_c}^{\hat{l}} \int_{\hat{l}}^{\hat{l}+2\hat{l}_p} \frac{{\varphi^3}_3(\hat{x},t)}{(1-w_{s3}(\hat{x}))^4} d\hat{x} \right] Dirac(\hat{x}-\hat{l}) \varphi_2 d\hat{x}$$
$$+\alpha_{fr} {V_{DC}}^2 \int_{\hat{l}_c}^{\hat{l}} \left[\int_{\hat{l}}^{\hat{l}+2\hat{l}_p} \frac{(\hat{x}-(\hat{l}+\hat{l}_p)){\varphi_3}^3}{(1-w_{s3}(\hat{x}))^4} d\hat{x} \right] \frac{\partial Dirac(\hat{x}-\hat{l})}{\partial \hat{x}} \varphi_2 d\hat{x}$$

$$M_4 = \int_0^{\hat{l}_c} \alpha_5 \varphi_1^2 d\hat{x} + \int_{\hat{l}_c}^{\hat{l}} \alpha_5 \varphi_2^2 d\hat{x} + \int_{\hat{l}_c}^{\hat{l}} \left[\int_{\hat{l}}^{\hat{l}+2\hat{l}_p} \hat{c}\varphi_3 \, d\hat{x} \right] Dirac(\hat{x}-\hat{l}) \varphi_2 d\hat{x}$$
$$- \int_{\hat{l}_c}^{\hat{l}} \left[\int_{\hat{l}}^{\hat{l}+2\hat{l}_p} \hat{c}(\hat{x}-(\hat{l}+\hat{l}_p))\varphi_2 \, d\hat{x} \right] \frac{\partial Dirac(\hat{x}-\hat{l})}{\partial \hat{x}} \varphi_2 d\hat{x}$$

$$M_5 = \int_0^{\hat{l}_c} \varphi_1^2 d\hat{x} + \int_{\hat{l}_c}^{\hat{l}} \varphi_2^2 d\hat{x} + \alpha_3 \int_{\hat{l}_c}^{\hat{l}} \varphi_2^2 \, Dirac(\hat{x}-\hat{l}) dx - \alpha_4 \int_{\hat{l}_c}^{\hat{l}} \left[\frac{\partial \varphi_2}{\partial \hat{x}} | \hat{x} = l \right] \frac{\partial Dirac(\hat{x}-\hat{l})}{\partial \hat{x}} \varphi_2 d\hat{x}$$

$$M_6 = -2\alpha_{el} V_{DC} \int_{\hat{l}_c}^{\hat{l}} \left[\int_{\hat{l}}^{\hat{l}+2\hat{l}_p} \frac{1}{(1-w_{s3}(\hat{x}))^3} d\hat{x} \right] Dirac(\hat{x}-\hat{l}) \varphi_2 d\hat{x}$$
$$+2\alpha_{el} V_{DC} \int_{\hat{l}_c}^{\hat{l}} \left[\int_{\hat{l}}^{\hat{l}+2\hat{l}_p} \frac{\left(\hat{x}-\left(\hat{l}+\hat{l}_p\right)\right)}{(1-w_{s3}(\hat{x}))^3} d\hat{x} \right] \frac{\partial Dirac(\hat{x}-\hat{l})}{\partial \hat{x}} \varphi_2 d\hat{x}$$
$$-2\alpha_{fr} V_{DC} \int_{\hat{l}_c}^{\hat{l}} \left[\int_{\hat{l}}^{\hat{l}+2\hat{l}_p} \frac{1}{(1-w_{s3}(\hat{x}))^2} d\hat{x} \right] Dirac(\hat{x}-\hat{l}) \varphi_2 d\hat{x}$$
$$+2\alpha_{fr} V_{DC} \int_{\hat{l}_c}^{\hat{l}} \left[\int_{\hat{l}}^{\hat{l}+2\hat{l}_p} \frac{(\hat{x}-(\hat{l}+\hat{l}_p))}{(1-w_{s3}(\hat{x}))^2} d\hat{x} \right] \frac{\partial Dirac(\hat{x}-\hat{l})}{\partial \hat{x}} \varphi_2 d\hat{x}$$

$$M_7 = -\alpha_{el}\int_{\hat{l}_c}^{\hat{l}}\left[\int_{\hat{l}}^{\hat{l}+2\hat{l}_p}\frac{1}{(1-w_{s3}(\hat{x}))^3}d\hat{x}\right]Dirac(\hat{x}-\hat{l})\varphi_2 d\hat{x} + \alpha_{el}\int_{\hat{l}_c}^{\hat{l}}\left[\int_{\hat{l}}^{\hat{l}+2\hat{l}_p}\frac{\left(\hat{x}-\left(\hat{l}+\hat{l}_p\right)\right)}{(1-w_{s3}(\hat{x}))^3}d\hat{x}\right]\frac{\partial Dirac(\hat{x}-\hat{l})}{\partial\hat{x}}\varphi_2 d\hat{x}$$
$$-\alpha_{fr}\int_{\hat{l}_c}^{\hat{l}}\left[\int_{\hat{l}}^{\hat{l}+2\hat{l}_p}\frac{1}{(1-w_{s3}(\hat{x}))^2}d\hat{x}\right]Dirac(\hat{x}-\hat{l})\varphi_2 d\hat{x} + \alpha_{fr}\int_{\hat{l}_c}^{\hat{l}}\left[\int_{\hat{l}}^{\hat{l}+2\hat{l}_p}\frac{(\hat{x}-(\hat{l}+\hat{l}_p))}{(1-w_{s3}(\hat{x}))^2}d\hat{x}\right]\frac{\partial Dirac(\hat{x}-\hat{l})}{\partial\hat{x}}\varphi_2 d\hat{x}$$

$$\begin{aligned}M_8 = &-2\alpha_{el}V_{DC}\int_{\hat{l}_c}^{\hat{l}}\left[\int_{\hat{l}}^{\hat{l}+2\hat{l}_p}\frac{\varphi_3}{(1-w_{s3}(\hat{x}))^3}d\hat{x}\right]Dirac(\hat{x}-\hat{l})\varphi_2 d\hat{x}\\ &+2\alpha_{el}V_{DC}\int_{\hat{l}_c}^{\hat{l}}\left[\int_{\hat{l}}^{\hat{l}+2\hat{l}_p}\frac{\left(\hat{x}-\left(\hat{l}+\hat{l}_p\right)\right)\varphi_3}{(1-w_{s3}(\hat{x}))^3}d\hat{x}\right]\frac{\partial Dirac(\hat{x}-\hat{l})}{\partial\hat{x}}\varphi_2 d\hat{x}\\ &-2\alpha_{fr}V_{DC}\int_{\hat{l}_c}^{\hat{l}}\left[\int_{\hat{l}}^{\hat{l}+2\hat{l}_p}\frac{\varphi_3}{(1-w_{s3}(\hat{x}))^2}d\hat{x}\right]Dirac(\hat{x}-\hat{l})\varphi_2 d\hat{x}\\ &+2\alpha_{fr}V_{DC}\int_{\hat{l}_c}^{\hat{l}}\left[\int_{\hat{l}}^{\hat{l}+2\hat{l}_p}\frac{(\hat{x}-(\hat{l}+\hat{l}_p))\varphi_3}{(1-w_{s3}(\hat{x}))^2}d\hat{x}\right]\frac{\partial Dirac(\hat{x}-\hat{l})}{\partial\hat{x}}\varphi_2 d\hat{x}\end{aligned}$$